Studies on the upgrade of the ALICE central tracker

Vom Fachbereich Physik
der Technischen Universität Darmstadt

zur Erlangung des Grades
eines Doktors der Naturwissenschaften (Dr. rer. nat.)

genehmigte Dissertation von
Dipl.-Phys. Magnus Mager
aus Wiesbaden

Darmstadt 2012

D 17

CERN

ALICE

TECHNISCHE
UNIVERSITÄT
DARMSTADT

Magnus Mager:
"Studies on the upgrade of the ALICE central tracker"
PhD thesis

Presented at:
Faculty of Physics
Technical University of Darmstadt
Darmstadt, Germany

Referent:
Prof. Dr. Peter Braun-Munzinger
(Technische Universität Darmstadt)
Korreferent:
Dr. Luciano Musa
(Europäische Organisation für Kernforschung, CERN)
Weiterer Gutachter:
Prof. Dr. Thomas Aumann
(Technische Universität Darmstadt)

Tag der Einreichung/date of submission: 22.06.2012
Tag der Prüfung/date of defence: 27.07.2012

dla Magdaleny

ZUSAMMENFASSUNG

Bei der Kollision von hochenergetischen Blei-Ionen, wie sie zur Zeit im "Großen Hadronen-Speicherring" (LHC) der "Europäischen Organisation für Kernforschung" (CERN) stattfinden, entstehen Energiedichten die denen gleichen, die kurz (ca. 1 ps bis 10 µs) nach dem Urknall herrschten. Sie bringen Materie in einen Zustand in dem die Bindung von Quarks in Hadronen verlorengeht und sie sich frei bewegen können – ein Plasma, das sogenannte Quark-Gluon-Plasma ensteht.

Dieses Bild bedarf nun einer gründlichen Prüfung und der neue Zustand will genaustes vermessen sein. Dazu müssen jedoch intrinsische Hürden überwunden werden: Die immense/makroskopische freie Energie, die diese Kollisionen mit sich bringen ($\approx$ 1 mJ), führt zu einer endlosen Zahl an möglichen Prozessen und schließlich – gemäß Massen-Energie Äquivalenz – zu einer rießigen Zahl (Ordnung 10 000) an erzeugten Teilchen.

Das ALICE Experiment wurde konstruiert um mit dieser Anzahl von Teilchen zurechtzukommen. Es kann die Eigenschaften (Impuls und Spezies) eines Großteils bestimmen. Dazu bedarf es einer sehr feinen Segmentierung des Detektors. Das Herz des Experiments bilden eine 90 m^3 große Spurenprojektionskammer (TPC), sowie ein Siliziumdetektor (ITS) nahe des Strahlrohres. Zusammen mit einem Flugzeitmassenspektrometer (TOF) bilden sie den "central tracker" und erlauben eine genaue Rekonstruktion des dreidimensionalen Spurbildes.

Die gemessenen Ereignisse bergen einen großen Informationsgehalt (ca. 700 MByte pro Ereignis), was wiederum hohe Anforderungen an die Auslese-Elektronik stellt. Um seltene Vorgänge messen zu können, müssen Milliarden von Kollisionen untersucht werden, was nach einer hohen Ausleserate (kHz) verlangt. Aber nicht nur die Ausleserate, sondern auch die räumliche Auflösung der Detektoren muss sehr hoch sein (wenige 10 µm), um z. B. Zerfälle von kurzlebigen Teilchen messen zu können.

Am Beispiel des Λ_c^+-Baryons, dem leichtesten Charm-Baryon, werden in der vorliegenden Arbeit die genaueren Implikationen für das Design von Detektoren analysiert. Die Messung des Λ_c^+ ist von großer Bedeutung für das Verständnis des Quark-Gluon Plasmas. Es enthält Informationen über den Charm-Sektor, insbesondere darüber wie Charm thermalisiert und/oder Energie im Plasma verliert. Zusammen mit Messungen aus dem mesonischen Charmsektor (D-Mesonen) lässt sich z. B. der Anteil der Up- und Down-Quarks von dem des Charm-Quarks an der Hadronisierung von Charm separieren.

Bis heute gibt es keine Messung des Λ_c^+ in zentralen Schwerionen-Kollisionen. ALICE hat das Λ_c^+ jedoch erfolgreich in Proton–Proton (p–p) messen können, was als wichtiger Vergleich dienen wird.

In dieser Arbeit werden Auflösung und Auslese-Rate der ALICE Detektoren analysiert und Vorschläge gemacht wie eine Messung des Λ_c^+ in Blei–Blei (Pb–Pb) Kollisionen möglich wird. Dazu wurden im Speziellen folgende Entwicklungen gemacht:

- Eine schnelle Analyse-Prozedur zur Analyse des Λ_c^+ Teilchens in p–p und Pb–Pb Kollisionen wurde entworfen, implementiert und erfolgreich mit den existierenden p–p Daten verwendet. Dies trug wesentlich zur Verbesserung der existierenden p–p Analyse bei (Kapitel 3). Zudem wurde die Analyse um die resonanten $\Lambda_c^+ \to pK^-\pi^+$, nämlich $\Lambda_c^+ \to \bar{K}^*(892)^0 p$, $\Lambda_c^+ \to \Delta(1232)^{++}K^-$ und $\Lambda_c^+ \to \Lambda(1520)\pi^+$, sowie die $\Lambda_c^+ \to K_S^0 p$ und $\Lambda_c^+ \to \Lambda\pi^+$ Zerfälle ergänzt.

- Die Auslese-Geschwindigkeit der existierenden Elektronik der TPC wurde systematisch analysiert. Ein Simulations-Model, sowie eine analytische Beschreibung der erreichbaren Raten wurde entwickelt. Basierend auf diesem Model wurde ein Vorschlag gemacht, wie sich durch eine Umstrukturierung des Auslesenetzwerks die derzeitigen Raten um einen Faktor Zehn steigern lassen. Um dies zu untermauern wurde eine Prototyp-Karte entwickelt und realisiert, die den kritischen Teil dieses Vorschlages ausmacht. Damit konnte demonstriert werden, dass dieser technisch umsetzbar ist (Kapitel 5).

- Basierend auf der Erfahrung mit der Analyse in p–p Kollisionen wurde analysiert, in wieweit eine Verbesserung des ITS die Messung des Λ_c^+ in Pb–Pb verbessert bzw. ermöglicht. Dazu wurde eine "hybrid" Monte-Carlo Methode entwickelt, die es erlaubt, schnell verschiedene Detektor-Geometrien miteinander zu vergleichen. Mit dieser konnte quantitativ gezeigt werden, wie ein Upgrade des ITS, zusammen mit einer schnelleren TPC, die Messung des Λ_c^+ in Pb–Pb ermöglicht (Kapitel 4). Diese Analyse und die entwickelte Methodik ist ein wesentlicher Bestandteil des derzeitigen ALICE Upgrade-Proposals.

ABSTRACT

When two high-energy lead ions collide, as they currently do inside the "Large Hadron Collider" (LHC) of the "European Organization for Nuclear Research" (CERN), energy densities similar to those shortly (some 1 ps to 10 µs) after the Big Bang are created. At these energies quarks are loosing their confinement into hadrons and may move around freely, the "quark-gluon plasma" (QGP) is created.

Such a picture deserves of course a thorough check and a precise measurement. There are however intrinsic difficulties to overcome: the macroscopic free energy (about 1 mJ) of these collision allow for an infinite number of processes to happen and finally—due to mass-energy equivalence—a significant number (order of 10 000) of particles is created.

The ALICE experiment was designed to be able to cope with this large number of particles, it can measure the properties (species and momentum) of the big majority. This requires a very fine segmentation of the detector. The central part of ALICE is made of a 90 m^3 time projection chamber (TPC), accompanied by a silicon detector close to the beam pipe (ITS). Completed by a time of flight detector (TOF) they form the "central" tracker. Together they measure the precise three-dimensional track picture of the collision.

The measured collision events produce a huge raw data volume of about 700 MByte, which sets tough requirements for the read-out electronics. To measure rare events one needs to record billions of collisions, which asks for high read-out rates (kHz). But also the spatial detector resolutions are required to be very good (a few 10 µm) in order to e. g. resolve decays of short-lived particles.

Taking the Λ_c^+ baryon, the lightest charmed baryon, as an example, the precise implications for the detector design are analysed in this thesis. Measuring the Λ_c^+ is of high importance for the understanding of the quark-gluon plasma. It bears valuable information on the charm sector, in particular on the charm thermalisation and/or energy loss in the plasma. Together with the measurements from the mesonic charm sector (D mesons) one may disentangle the contributions of u and d quarks to the hadronisation process from those caused by c quarks.

Till today there is no data from Λ_c^+ production in central heavy-ion events available. ALICE has however successfully measured the Λ_c^+ yield in proton–proton (p–p) collisions, which will serve as a valuable cross-check.

In the frame of this thesis the following developments were carried out:

- A fast analysis procedure for the Λ_c^+ in p–p and Pb–Pb collisions was designed, implemented and successfully tested with existing p–p data (Chap. 3). This did not only prove the method to be working but also helped to improve the currently employed analysis code for p–p. Also were the resonant $\Lambda_c^+ \to pK^-\pi^+$ channels, namely $\Lambda_c^+ \to \bar{K}^*(892)^0 p$, $\Lambda_c^+ \to \Delta(1232)^{++}K^-$,

and $\Lambda_c^+ \to \Lambda(1520)\pi^+$, as well as the $\Lambda_c^+ \to K_S^0 p$ and $\Lambda_c^+ \to \Lambda\pi^+$ decay modes added to the analysis.

- The read-out speed of the existing TPC electronics was analysed systematically and a simulation model as well as an analytic treatment of the obtainable rates were developed. Based on this model a proposal to reorganise the read-out network is made, which can improve the speed by a factor of ten. To prove its feasibility, a prototype card of the main part of the network was designed and realised, which proves the critical part and the technical feasibility of this proposal (Chap. 5).

- Based on the experience with the analysis of p–p collisions it was investigated how far an improvement of the ITS will translate into an improvement of the Λ_c^+ measurement. For this purpose a "hybrid" Monte-Carlo method was developed that allows to quickly compare different detector geometries. With this method it could be quantitatively shown how an upgrade of the ITS together with an improved read-out network for the TPC allow to measure the Λ_c^+ in Pb–Pb (chapter 4). This analysis and the developed methodology are a main contribution to the current ALICE upgrade strategy.

CURRICULUM VITAE—MAGNUS MAGER

	Education
2003–2008	Studies of physics & mathematics at the Technical University of Darmstadt, Germany
2005	Intermediate diplomas in physics & mathematics
2005–2006	Year abroad at the Technical University of Warsaw, Poland
2007–2008	Diploma thesis (physics) at the Gesellschaft für Schwerionenforschung mbH (GSI), Darmstadt, Germany, title: "Spatial Calibration of the ALICE TPC Field Cage and First Physics Ideas"
2008	Diploma in physics
2008–2012	PhD student at the European Organization for Nuclear Research (CERN), Geneva, Switzerland
	Internships/Work
2002	Four-week internship at the International Institute for Molecular and Cell Biology, Warsaw, Poland
2002–2003	Alternative civilian service at the German Red Cross, Wiesbaden, Germany
2003–2010	Embedded systems developer at stoll-digital-elektronik, Wiesbaden, Germany
	Scholarships/Awards
2002	Award of the Karin-Elisabeth-Loos foundation, Wiesbaden, Germany
2005–2006	Erasmus scholarship for year abroad
2006–2008	Scholarship of the German National Academic Foundation (Studienstiftung des Deutschen Volkes)
2008–2011	Wolfgang Gentner scholarship for a three-years stay at CERN within its doctoral student program
2011	Poster award at the "Technology and Instrumentation in Particle Physics 2011" conference, Chicago, Illinois, USA (see also [MM8])
2011	"Patrick M. S. Blackett Diploma" & "New Talent Award" at the "International School of Subnuclear Physics", Erice, Italy (see also [MM9])
2012–	CERN COFUND fellowship

PUBLICATIONS

As a member of the ALICE collaboration the author is co-author of all physics publications since the startup of LHC published by the ALICE experiment. The following list consists of additional publications that the author has contributed to.

[MM1] F. Frohns, M. Mager and P. G. Layer. *Basic fibroblast growth factor increases the precursor pool of photoreceptors, but inhibits their differentiation and apoptosis in chicken retinal reaggregates*. In: *Eur. J. Neurosci.* 29.10 (2009), pp. 1931–1942. DOI: 10.1111/j.1460-9568.2009.06738.x.

[MM2] M. Mager (for the ALICE TPC Collaboration). *The commissioning of ALICE's TPC*. In: *Physics at the LHC*. DESY, 2010. DOI: 10.3204/DESY-PROC-2010-01/193.

[MM3] ALICE TPC Collaboration. *The ALICE TPC, a large 3-dimensional tracking device with fast readout for ultra-high multiplicity events*. In: *Nucl. Instr. Meth.* A622.1 (2010), pp. 316–367. DOI: 10.1016/j.nima.2010.04.042. arXiv:1001.1950 [physics.ins-det].

[MM4] A. Junique et al. *Upgrade of the ALICE-TPC read-out electronics*. In: *Topical Workshop on Electronics for Particle Physics*. Vol. 5. 12. 2010, p. C12026. DOI: 10.1088/1748-0221/5/12/C12026.

[MM5] M. Mager, S. Rossegger and J. Thomas. *The Langevin equation expanded to 2nd order and comments on using the equation to correct for space point distortions in a TPC*. ALICE internal note, ALICE-INT-2010-016. 2010. URL: https://edms.cern.ch/document/1108138/1/.

[MM6] M. Mager, S. Rossegger and J. Thomas. *Composed correction framework for modeling the TPC field distortions in AliRoot*. ALICE internal note, ALICE-INT-2011-002. 2011. URL: https://edms.cern.ch/document/1113105/1.

[MM7] M. Mager et al. (for the ALICE TPC Collaboration). *Measurement of single event upsets in the ALICE-TPC front-end electronics*. In: *Appl. Mech. Mater.* 110 (2011), pp. 4505–4511. DOI: 10.4028/www.scientific.net/AMM.110-116.4505. arXiv:1110.3232 [physics.ins-det].

[MM8] C. Horn et al. (for the ALICE TPC Collaboration). *Trigger-induced mechanical resonances of gating grid wires in the multi-wire proportional chambers of the ALICE TPC*. In: *Proceedings of TIPP 2011*. 2012 (accepted for publication in Phys. Procedia). DOI: 10.1016/j.phpro.2012.02.395 (cit. on p. ix).

[MM9] M. Mager (for the ALICE TPC Collaboration). *Mechanical resonances in the read-out chambers of the ALICE TPC*. In: *Proceedings of ISSP 2011*. to be published in World Scientific, 2012 (cit. on p. ix).

CONTENTS

1

INTRODUCTION

ALICE "A Large Ion Collider Experiment" is the most recent experiment that studies collisions of heavy ions at ultra-relativistic energies, where its main objective is the detailed characterisation of the quark-gluon plasma. In this regard, a rich physics programme is currently carried out, studying various aspects of this exotic state of matter. In this thesis one very important—but also challenging—measurement is discussed: the measurement of the Λ_c^+ yield.

1.1 THE QUARK-GLUON PLASMA

Quantum chromo dynamics (QCD)[1] is the theory of the standard model of particle physics. It describes the interactions between quarks and gluons and explains why no free quarks are observed, which is termed "confinement" (which is a result form lattice QCD calculations). It also predicts where and how quarks can be found in nature. The different possible configurations can be summarised in a phase diagram (Fig. 1), from which one sees that indeed distinct regimes (phases, like in "ordinary" thermodynamics) are predicted.

The quark-gluon plasma (QGP) is the state of matter in which quarks and gluons are deconfined, i. e. where they are not bound into hadrons but may move around freely. It is assumed that this was the state of our universe shortly after it had been born with the Big Bang (at the age of 1 ps to 10 µs)—and it is the state that is created in collisions of high-energy heavy ions as they currently happen at the Large Hadron Collider (LHC). The latter setting is under better control and offers the unique opportunity to carefully measure properties of the QGP[2].

1.2 HEAVY FLAVOUR PROBES

The challenge with QGP is that one cannot observe it directly, but only sees what is left over after it has undergone the (phase) transition to hadronic matter. Now,

1 See e. g. [2] for an introduction.
2 Good textbooks on the topic are [3, 4] (experimental) and [5] (more theoretical).

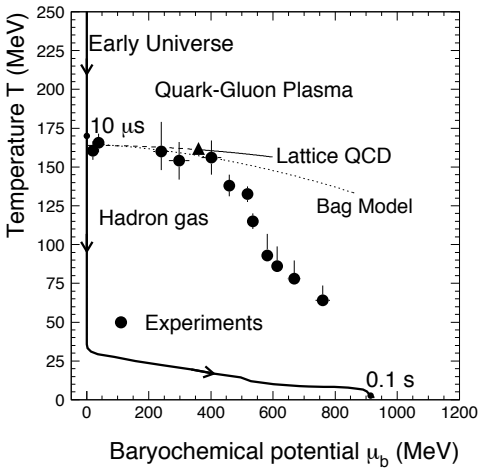

Figure 1: The phase diagram of QCD. Figure reproduced from [1].

if one assumes that a real phase transition occurred, at this point in time, most particles have thermalised and lost valuable information about the QGP.

There are the macroscopic properties of the created plasma that can be measured, like its emission size (radii of 6 fm to 8 fm [6]), its expansion geometry ("flow" [7]), or its freeze-out temperature (about 148 MeV to 165 MeV [8]). But they do not reveal much about the mechanisms at work inside the plasma. In order to measure the dynamics of the plasma one needs probes that are "calibrated" in the sense that one knows their properties in case that there is no QGP. In that way one can measure how they are affected by interactions with the medium.

From the direct photon measurement of PHENIX[3] (Au–Au at $\sqrt{s_{NN}} = 200$ AGeV), one obtains an average QGP temperature scale of the order of some 230 MeV [9]. While till now no measurement from LHC is available, scaling arguments show that the temperature is in the range of 500 MeV [10], large enough to create $u\bar{u}$, $d\bar{d}$, and also enough $s\bar{s}$ quark pairs, but certainly too little as to create $c\bar{c}$ or even heavier pairs. One calls the former "light quarks" and the latter "heavy quarks", respectively, and assumes that members of the latter are only created in the initial hard collisions of nucleons, that is before the QGP is created. In order words, c quarks are calibrated probes. Their properties (cross-sections) can be measured in (QGP-free) p–p collisions and extrapolated to Pb–Pb initial state conditions (before creation of QGP) using the Glauber model[4].

Since the abundances of heavy quarks are limited to a few, the likelihood that they will meet each other in order to annihilate is low [12]. The time until they would decay weakly is large (as compared to the QGP lifetime) and eventually

3 PHENIX is "A Physics Experiment at RHIC", the "Relativistic Heavy Ion Collider".

4 The Glauber model is a simple model of the collision that assumes that the Pb–Pb collision is an incoherent superposition of nucleon–nucleon collisions [11].

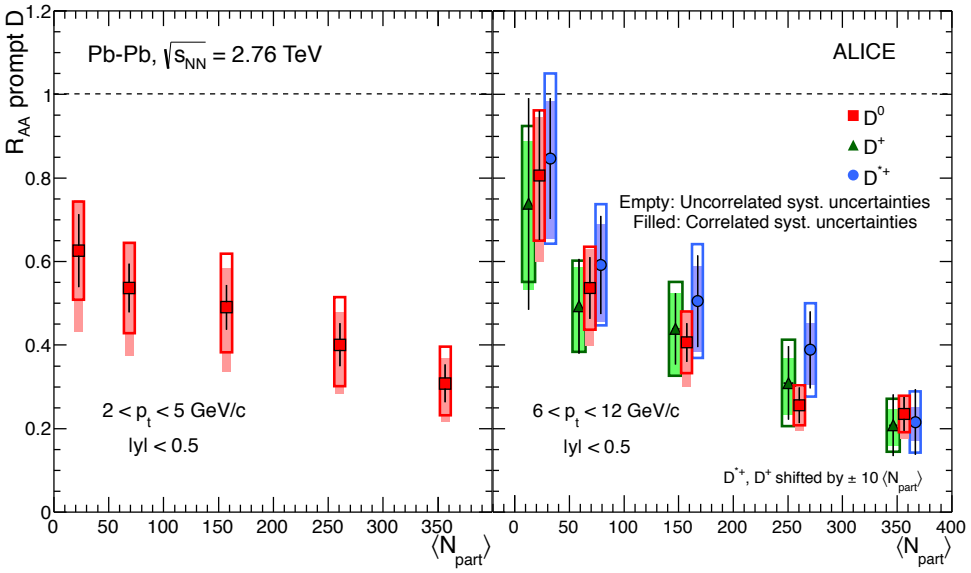

Figure 2: R_{AA} for different charmed mesons as measured by ALICE in $\sqrt{s_{NN}} = 2.76$ ATeV collisions. Figure reproduced from [14].

they are forced to pair up with light quarks (which are abundant) and to form hadrons when the phase transition from QGP to hadronic matter ("chemical freeze out") happens. Here charm fragments into the different hadrons, the bulk goes into singly charmed mesons (mainly D^0, D^+, D_s) and baryons (mainly Λ_c^+). Apart from this "open charm", there is also a small fraction going into $c\bar{c}$ pairs, "hidden charm" (mainly J/ψ)[5].

Experimentally the difference between the superposition of nucleon–nucleon collisions on the one hand and nucleus–nucleus collisions on the other hand is captured in the nuclear modification factor, R_{AA}, which is the correctly scaled ratio of Pb–Pb over p–p cross-sections of an observable, e. g. the yield of charmed mesons in a certain phase space region. The latter has recently been measured by ALICE (Fig. 2) and can directly be compared to predictions from different models of the QGP [14].

If the previous reasoning is correct, and the total number of charmed hadrons stays constant, the only possible conclusions from Fig. 2 are that its $p_\perp$ spectrum has either shifted drastically towards low momenta or that the charm fragmentation fractions in Pb–Pb are very different from those in p–p, for example that more charm goes into Baryons. A higher baryon yield does not even seem too unlikely given the vast amount of light quarks floating around in the QGP.

5 For completeness: There are also multiply charmed baryons predicted (e. g. Ω_{ccc} [13]), but their production probability much lower. Moreover, that the bulk goes into mesons is of course an assumption, until it has been experimentally verified. It is true, however, for all other previously studied systems, see Sec. 2.1.2.

1.3 ALICE

The Large Hadron Collider (LHC) operated at CERN in Geneva, Switzerland is the most powerful particle accelerator available today. It accelerates and collides protons ("p–p") at centre-of-mass energies of up to $\sqrt{s} = 7\,\mathrm{TeV}$ as well as lead ions ("Pb–Pb") at centre-of-mass energies per nucleon of $\sqrt{s_{\mathrm{NN}}} = 2.76\,\mathrm{ATeV}$, and plans are to increase these energies to their design values of 14 TeV and 5.5 ATeV, respectively [15].

At the different beam configurations and these unprecedented energies a lot of "new physics" is expected to happen and correspondingly a comprehensive physics program is carried out by different experiments along the accelerator ring. This thesis focusses on one of the four big experiments at LHC: ALICE, "A Large Ion Collider Experiment", which is devoted to the characterisation of heavy-ion collisions [16].

The macroscopic amount of 0.1 mJ of kinetic energy is available in a $\sqrt{s_{\mathrm{NN}}} = 2.76\,\mathrm{ATeV}$ Pb–Pb collision allows for a vast amount of particles to be created. Indeed, the number of charged particles per unit of pseudorapidity[6] is measured to be $\mathrm{d}N_{\mathrm{ch}}/\mathrm{d}\eta|_{\eta=0} \approx 1600$ for the most central of such collisions [17]. In order to be able to resolve the collision topology, to identify the emerging particles, and in order to measure their properties a very finely segmented detector with high resolution is needed.

1.3.1 *Sub-detectors*

ALICE was designed as a many-purpose detector. It can be divided into the central barrel and the muon system (at large pseudorapidities), both of which in turn can be further subdivided into several sub-detectors (Fig. 3).

Most of the sub-detectors serve specific purposes [16, 19] and for the reminder of this work, only a small subset plays an important role. Theses are (in order of increasing radial distance from the interaction region):

- ITS, "Inner Tracking System": six layers of silicon detector for precise tracking and vertex reconstruction [20].
- TPC, "Time Projection Chamber": high granularity tracking and particle identification via specific energy loss [21, 18].
- TOF, "Time-Of-Flight": particle identification via flight time measurement [22, 23].

6 Pseudorapidity is a measure of angle: $\eta := -\ln\tan(\theta/2)$, with θ being the polar angle wrt. the beam direction.

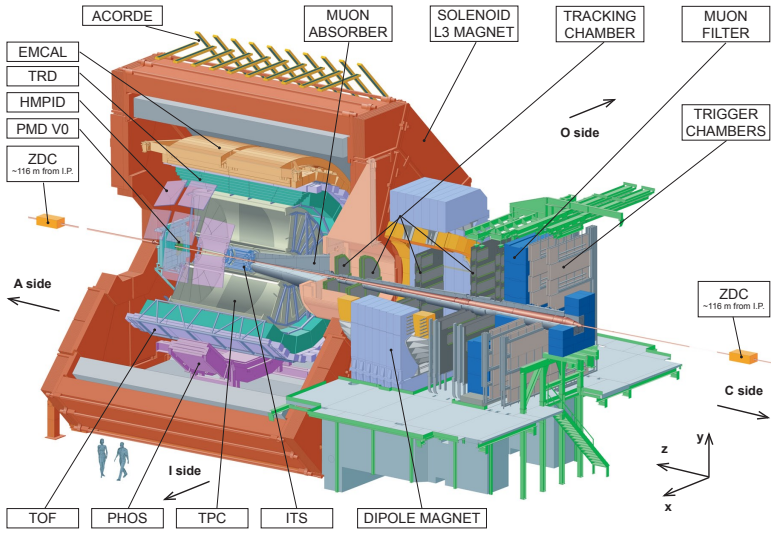

Figure 3: Layout of ALICE detector set-up, showing its division into sub-detectors. Figure taken from [18].

1.3.2 *Key features*

There are essentially two features that distinguish ALICE from the other LHC experiments [24]:

- Good momentum resolution down to low transverse momenta due to the low material budget of its detectors. Both the ITS and especially the TPC are very light in terms of radiation length. This translates into an excellent momentum resolution (due to little multiple scattering). In addition the experiment is placed in a moderate magnetic field of only 0.5 T, which results in larger bending radii and thus higher acceptance for low momentum particles.

- Excellent particle identification (PID). ITS, TPC, and TOF contribute to the identification of the particle species. Two different identification mechanisms, specific energy loss and time of flight, are employed. Combined they resolve ambiguities and provide a decisive PID over a wide momentum range.

These two features are of utmost importance for the measurements of the $p_\perp$-differential cross-sections of charmed hadrons, since they help to reduce the combinatorial background drastically and because most of their cross-section is found at low transverse momenta.

1.3.3 *The p–p reference data of 2010*

In the year 2010 ALICE recorded p–p collisions, mainly as a future reference for Pb–Pb. The collected data sample consists of $N_{\mathrm{MB}} = 382\,712\,096$ minimum bias $\sqrt{s} = 7\,\mathrm{TeV}$ p–p events[7], which corresponds to an integrated luminosity of $L_{\mathrm{int}} = N_{\mathrm{MB}}/\sigma_{\mathrm{MB}} = 6.14\,\mathrm{nb}^{-1}$, with the inelastic cross-section, $\sigma_{\mathrm{MB}} = 62.3\,\mathrm{mb}$, as obtained from a van-der-Meer scan [25].

The events are triggered using a minimum-bias trigger that is based on the coincidence of a bunch crossing with a signal in the ITS or VØ detectors. Afterwards a quality selection of the events is applied in the analysis code to reject pile-up events. This procedure is common to all central barrel p–p analyses published so far, for details see e. g. [26].

1.3.4 *Pb–Pb data sample*

Two months of LHC operation (December 2010 and December 2011) were dedicated to the collection of Pb–Pb collisions at $\sqrt{s_{NN}} = 2.76\,\mathrm{ATeV}$. The first data set consists of minimum bias events to address the bulk properties of the medium, while as in 2011 more refined triggers were used to collect more events in interesting centrality regions. The 2010 data has been calibrated well by now and forms the basis for all ALICE Pb–Pb results quoted in this thesis, while as the analysis of 2011 data is still in progress by the time of this writing.

1.3.5 *Upgrade*

The analysis the first of Pb–Pb data has already produced two very interesting results that are of importance for this thesis:

- The D meson R_{AA} shows that a big part of the presumably produced charm is currently not found in the form of D mesons [14].
- D hadrons show collective behaviour, they "have flow" [27].

Neither is well understood and both need further experimental investigation. In particular it is crucial to measure all charmed particles, explicitly including the baryonic part and to extent the measurements to low transverse momenta.

This will not only limit the systematic uncertainties entering the measurements quoted above but also allows to cross-checks its interpretations (see Chap. 4 and [28] for more details).

The ALICE collaboration has therefore decided to pursue an upgrade of the detector, which will allow to carry out the necessary measurements. The upgrade targets at two main improvements: an increase of measurement precision and an increase of event-rate.

7 In ALICE terminology: run periods "LHC10b", "LHC10c", "LHC10d", and "LHC10e".

This thesis is framed within this common undertaking and develops the first quantitative proposals of how these goals could be achieved. The methods and results that are laid out in the upcoming chapters are a major input to the official ALICE upgrade documents [28, 29].

2

THE Λ_c^+ PARTICLE

This thesis is built around the analysis of Λ_c^+ particles[1]. The Λ_c^+ particle is the lightest charmed baryon, with quark content $\Lambda_c^+ = udc$ and mass $m_{\Lambda_c^+} = 2.286\,46(14)\,\mathrm{GeV}/c^2$. It is short-lived, $c\tau = 59.9\,\mu\mathrm{m}$, and decays via a large variety of different modes (all of which have small relative fractions) [30]. It has been studied thoroughly in e^+–e^- collisions, but little is known from more complicated systems—for reasons that will become clear below.

2.1 PRODUCTION

Being a hadron the formation of the Λ_c^+ is described by QCD, in principle. Unfortunately the hadronisation is a non-perturbative process and as such its evaluation is extremely complicated. Simplified models have been developed to make the problem more accessible. Here a few of them are summarised.

2.1.1 *Thermal production*

In the framework of the statistical hadronization model (SHM, see [12] and references therein), all hadrons are formed at the chemical freeze-out according to their statistical weights. Hereby the discrete quantum numbers of the initial state state of the colliding system need to be conserved. Assuming that charm quarks are sparse enough such that no annihilation occurs, this includes their total number, which must stay constant. In particular, carrying out this calculation yields a prediction for the integrated Λ_c^+/D^0 ratio of 0.163(16) [31].

2.1.2 *Fragmentation fractions*

Once charmed quarks are produced they at some point have to hadronise (due to confinement), i. e. somehow find partners to form hadrons. How this happens is unknown, it is a non-perturbative effect but it is assumed to be common for all systems. This leads to the definition of "fragmentation fractions", which tell how much charm goes into which hadron species. It is an experimentally quantity that

1 Throughout this thesis "Λ_c^+" stands for the sum of particles (Λ_c^+) and antiparticles ($\bar{\Lambda}_c^-$).

(currently) cannot be calculated but has been measured in different systems and the assumption of being system independent is compatible within (large) errors. For the part $f(c \to \Lambda_c^+)$ these errors are of the order of 50 % and the means range from 7.6 % (in e^+–e^- collisions) to 14.4 % (in photo production). A summary is given in Tab. 1.

2.1.3 *Feed-down*

Heavier particles may decay into Λ_c^+. In particular the decays of type "$\Lambda_b^0 \to \Lambda_c^+ l^- \bar{\nu}_l + \text{anything}$" contribute largely. In Pb–Pb collisions at LHC energies, the relative contribution of these decays to the total Λ_c^+ yield is not negligible, as the $b\bar{b}$ cross-section becomes large [24]. When calculating the cross-section of charm hadrons these contributions have to be carefully taken into account. This currently imposes quite some difficulty since the beauty cross-sections are not well known themselves. One aim of the upgrade will therefore also be to measure them in order to reduce the systematic error of the charm measurements.

2.1.4 *Monte-Carlo: HIJING*

For the purpose of the further discussions a "realistic" sample of Λ_c^+ particles is needed. This can best be obtained by the use of Monte-Carlo generators.

For the discussion on Pb–Pb in Chap. 4, a HIJING [36] based Mont-Carlo was used. The $p_\perp$ spectrum of the produced Λ_c^+ particles is shown in Fig. 4. It can be well fitted with a thermal spectrum, i. e. one with invariant cross-section of type:

$$\frac{1}{p_\perp}\frac{\mathrm{d}N}{\mathrm{d}y\mathrm{d}p_\perp} \propto \exp(-p_\perp/T) \tag{2.1}$$

with $T = 1.17\,\mathrm{GeV}$.

Table 1: The charm fragmentation fractions as measured by different experiments. Especially the Λ_c^+ part has a very large error.

	γp (ZEUS [32])			DIS (ZEUS [33])			DIS (H1 [34])	e^+e^- (comb. [35])	
	stat.	syst.	br.	stat.	syst.	br.	total	stat.+syst.	br.
$f(c \to D^+)$	0.217	± 0.014	$^{+0.013}_{-0.005}$ $^{+0.014}_{-0.016}$				0.203 ± 0.026	0.226 ± 0.010	$^{+0.016}_{-0.014}$
$f(c \to D^0)$	0.513	± 0.021	$^{+0.018}_{-0.017}$ $^{+0.022}_{-0.032}$				0.560 ± 0.046	0.557 ± 0.023	$^{+0.014}_{-0.013}$
$f(c \to D_s^+)$	0.095	± 0.008	$^{+0.005}_{-0.005}$ $^{+0.026}_{-0.017}$				0.151 ± 0.055	0.101 ± 0.009	$^{+0.020}_{-0.034}$
$f(c \to \Lambda_c^+)$	0.144	± 0.022	$^{+0.013}_{-0.022}$ $^{+0.037}_{-0.025}$	0.117	± 0.033	$^{+0.026}_{-0.022}$ $^{+0.027}_{-0.027}$		0.076 ± 0.007	$^{+0.027}_{-0.016}$
$f(c \to D^{*+})$	0.200	± 0.009	$^{+0.008}_{-0.006}$ $^{+0.008}_{-0.012}$				0.263 ± 0.032	0.238 ± 0.007	$^{+0.003}_{-0.003}$

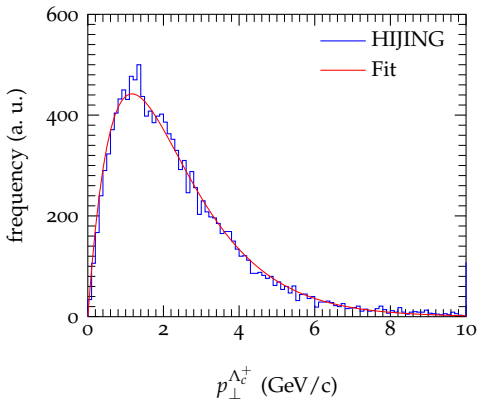

Figure 4: HIJING Λ_c^+ $p_\perp$ spectrum. See text for details.

2.2 DECAY

After an average Eigen-time of only $200(6) \times 10^{-15}$ s ($c\tau = 59.9\,\mu$m) the Λ_c^+ decays[2]. A large variety of decay channels are known and all of them have small branching ratios [30]. The most promising decay modes for an analysis with ALICE are summarised in Tab. 2 and discussed hereunder.

2 It should be noted, that the distance a particle of mass m and with momentum $\vec{p}$ travels in Eigen-time τ is $|\vec{l}| = \beta c\gamma\tau = (|\vec{p}|/m)\tau$, i. e. it is largely dependent on the momentum. For the Λ_c^+ typically momenta are of the order of its mass (thermal spectrum), such that $c\tau$ gives a good idea of the commonly observed decay lengths.

Table 2: Summary of used decays channels and their respective branching ratios into the observed final states (ratios calculated from [30]).

Mode	Fraction (%)	Decay length (cm) (intermediate particle)
$\Lambda_c^+ \to pK^-\pi^+$ (total)	5.0 ± 1.3	—
$\Lambda_c^+ \to (\Lambda(1520) \to p\ K^-)\pi^+$	0.41 ± 0.13	prompt
$\Lambda_c^+ \to (\Delta(1232)^{++} \to \pi^+ p\ )K^-$	0.86 ± 0.30	prompt
$\Lambda_c^+ \to (\bar{K}^*(892)^0 \to K^-\pi^+)p$	0.80 ± 0.25	prompt
$\Lambda_c^+ \to pK^-\pi^+$ (non-resonant)	2.8 ± 0.8	—
$\Lambda_c^+ \to (K_S^0 \to \pi^+\pi^-)p$	0.80 ± 0.21	2.68
$\Lambda_c^+ \to (\Lambda \to p\ \pi^-)\pi^+$	0.68 ± 0.18	7.89

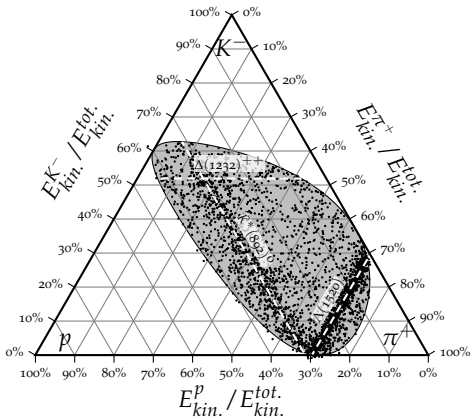

Figure 5: Dalitz plot of the $\Lambda_c^+ \rightarrow pK^-\pi^+$ decay showing the resonant decay modes. The plot is based on reconstructed MC data (the branching fractions have been adapted for better visibility).

2.2.1 $\Lambda_c^+ \rightarrow pK^-\pi^+$

The three-body decay of the Λ_c^+ into the proton, kaon, pion final state is the decay channel used in most Λ_c^+ analyses and also is the reference channel for other branching ratios [30, Λ_c^+ branching fractions review]. Its main advantages are:

- large branching ratio: 5.0(13) % (large statistics)
- "only" three decay products (reduces combinatorics)
- all decay products are charged (makes them directly detectable in the tracking detectors)
- all decay products are long-lived (no need to reconstruct subsequent decays)
- only one pion within the decay products (greatly reduces the combinatorics)

Resonant substructure ($\Lambda(1520)$, $\Delta(1232)^{++}$, $\bar{K}^*(892)^0$)

The decay into the three-body final state may happen via an intermediate resonant two-body state. One resonant state for each of the three two body combinations is known [30]; they are listed with their respective fractions in Tab. 2. One way to depict these resonances is a Dalitz-plot [37], a ternary scatter plot indicating the splitting of total energy in the Λ_c^+ rest frame onto the three decay products. A feature of the plot is that in terms of production probability it is flat if the decay is non-resonant, i. e. all points within the kinematic limits are equally likely. Resonances appear as lines parallel to the axis connecting the two daughter particles. Fig. 5 shows such a plot for the Λ_c^+ particle.

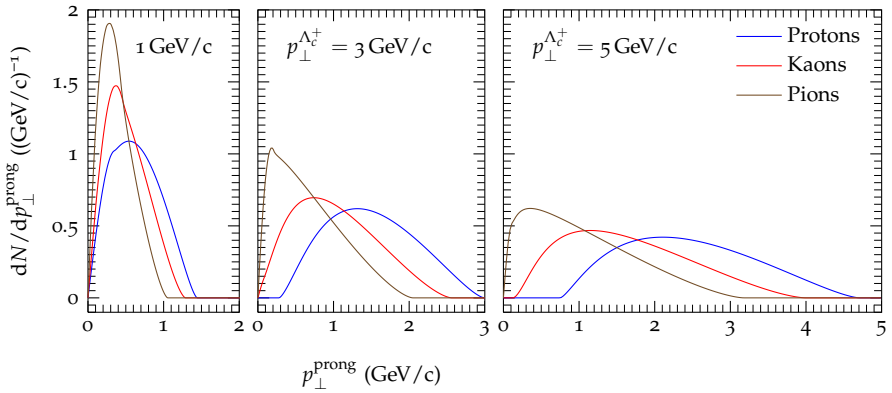

Figure 6: The $p_\perp$ spectra of the $\Lambda_c^+ \to pK^-\pi^+$ decay products for three values of the Λ_c^+ $p_\perp$.

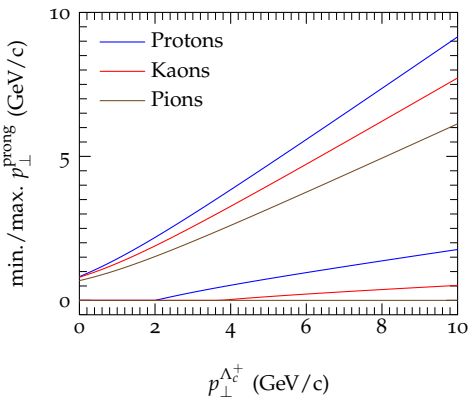

Figure 7: The allowed $p_\perp$ ranges of the $\Lambda_c^+ \to pK^-\pi^+$ decay products depending on the Λ_c^+ $p_\perp$. NB: they are not independent.

Kinematics

Apart from rotational symmetry of the decay frame, the complete kinematics is contained in the Dalitz plot. The measured properties of the decay products, in particular their $p_\perp$ spectra, can be obtained by integrating over the allowed phase space. A few examples are shown in Fig. 6. It can be seen that the kinematics allow only a certain range of prong $p_\perp$ for a given Λ_c^+ $p_\perp$. These limits are summarised in Fig. 7. When interpreting the plots it should be noted that the $p_\perp$ of the three prongs are not independent.

The phase space element $\mathrm{d}\Gamma$ of the three-body decay can be written as [30]:

$$\mathrm{d}\Gamma = \frac{1}{(2\pi)^3}\frac{1}{8m_{\Lambda_c^+}}\overline{|\mathfrak{M}|^2}\mathrm{d}E_1\mathrm{d}E_2 \,, \tag{2.2}$$

with the spin-averaged matrix element $\overline{|\mathfrak{M}|^2}$. This distribution is flat in the energies of any two prongs, E_1 and E_2, in the rest frame of the Λ_c^+.

From the conservation of 4-momenta, the following relation between energy of one particle in the rest frame of the Λ_c^+, E_k, and the 4-momenta of the two others, p_i and p_j, can be established:

$$E_k = \frac{m_{\Lambda_c^+}^2 + m_k^2 - (p_i + p_j)^2}{2m_{\Lambda_c^+}} = \frac{m_{\Lambda_c^+}^2 + m_k^2 - m_{ij}^2}{2m_{\Lambda_c^+}} \,, \tag{2.3}$$

in particular:

$$\mathrm{d}E_k = -\mathrm{d}m_{ij}^2 \,. \tag{2.4}$$

This shows that the Dalitz plot can also be drawn in the simple-to-measure quantities, $m_{ij}^2 = (p_i + p_j)^2$, the two-particle masses squared. In Fig. 5, the kinetic energies ($E_{\text{kin.}}^i = E_i - m_i$) were chosen.

2.2.2 $\Lambda_c^+ \to V^0 + x^+$

Another interesting set of decay modes are those that decay via a neutral strange particle (either a K_S^0 or a Λ), which themselves decay into two charged particles after a few cm of lifetime (V^0-like decay). There are some drawbacks when comparing to the $pK^-\pi^+$ channel:

- The branching ratio is smaller.
- The intermediate neutral particle is not tracked itself but needs to be reconstructed from its decay products.
- The neutral particle decays into modes of which not all are well observable in ALICE. This reduces the effective branching ratio further.
- Also these decays all have a $p\pi^+\pi^-$ final state, i. e. they have a larger combinatorial background due to the presence of two pions.

The big advantage, however, is the possibility to apply a selection based on the neutral particle: the displacement of its decay vertex, its reconstructed mass as well as the fact that it is pointing to the decay of the Λ_c^+ can be used to distinguish signal from background.

$\Lambda_c^+ \to K_S^0 p$

The decay into K_S^0 and proton is the cleanest decay mode available, as both the K_S^0 and the proton can be identified very well. This is due to the fact that the number of protons originating from the primary vertex is much smaller than the number of pions and also smaller than the number of kaons. Moreover can the proton be identified well by both the TPC and TOF for the relevant momentum rage. The pions from the K_S^0 decay have the advantage of being significantly displaced from the primary vertex. Here the analysis is carried out using the $K_S^0 \to \pi^+\pi^-$ decay mode (branching-ratio: 69.2 %).

$\Lambda_c^+ \to \Lambda\pi^+$

The second alternative is the decay via the Λ baryon and its subsequent decay into $p\pi^-$ (branching ratio: 63.9 %). It is more difficult, because the pion from the Λ_c^+ is harder to sieve out of the large yield of primary pions. Also does the Λ decay further away, hence it is more often affected by multiple scattering at the beam pipe and ITS layers.

In the analysis of this mode care has to be taken because of a reflection appearing in the background due to the decay $\Lambda_c^+ \to \Sigma^0\pi^+$ and the subsequent decay of $\Sigma^0 \to \Lambda\gamma$ with a very soft photon. More details in Appendix A.

2.3 RESULTS FROM OTHER EXPERIMENTS

Most studies of the Λ_c^+ particle were carried out at lepton colliders. Little is known about its production in other systems. At HERA[3], the charm fragmentation into Λ_c^+ was measured in two other systems: in photo production ("γp") [32] and in deep inelastic scattering (DIS) [33]. While comparable within errors to the results from $e^+ - -e^-$ [35] (see also Tab. 1), the results vary by a factor of two, and thus do not really tell if charm fragmentation is independent of the analysed systems.

In addition B-factories measured the Λ_c^+, as a decay product of the Λ_b decays, which allow to study its decay but do not give much inside regarding production.

For completeness, the only known measurements from hadron colliders are from p–p collisions [38] as well as from π^-–Cu and K^-–Cu [39] collisions at SPS[4].

Here the raw mass spectra from ZEUS for γp (Fig. 8) and DIS (Fig. 9) are shown for completeness. They use the $pK^-\pi^+$ and V^0x^+ decay channels, respectively, for their analyses, i. e. precisely those that are used in this thesis as well. Especially Fig. 9b shows how difficult the signal extraction becomes in more complex systems.

3 Two experiments called "ZEUS" and "H1" at HERA, the "Hadron-Electron Ring Accelerator" at the Deutsches Elektronen-Synchrotron (DESY), measured the charm fragmentation fractions.

4 SPS is the "Super Proton Synchrotron", an accelerator at CERN

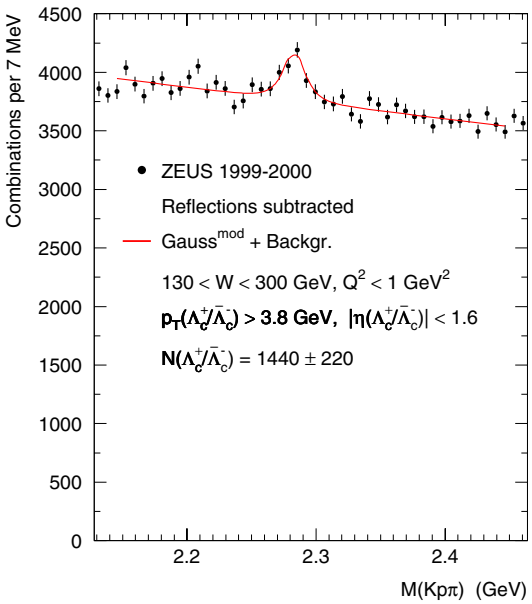

Figure 8: The ZEUS mass spectra for $\Lambda_c^+ \to pK^-\pi^+$ in γp. Figure reproduced form [32]

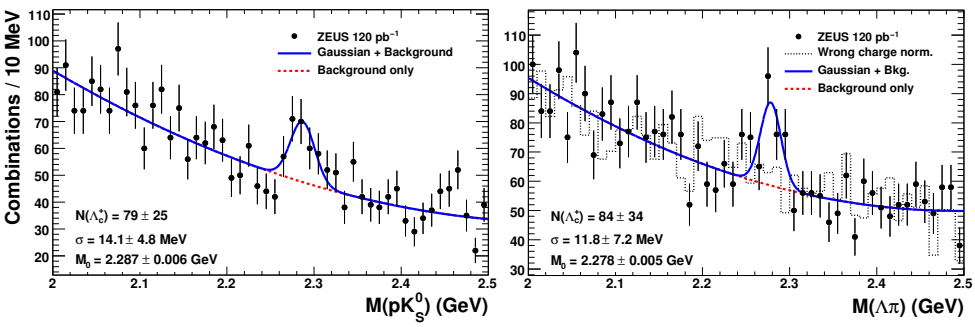

(a) $\Lambda_c^+ \to K_S^0 p$ (b) $\Lambda_c^+ \to \Lambda\pi^+$

Figure 9: The ZEUS mass spectra for $\Lambda_c^+ \to V^0 x^+$ in DIS. Figures reproduced form [33]

2.4 OPEN QUESTIONS

No direct Λ_c^+ measurements exist for heavy-ion collisions. However, it is known that its precise abundance will affect other measurements. There, its production has to be postulated "somehow" and consequently is responsible for systematic uncertainties. Moreover, the baryonic nature of the Λ_c^+ allows to verify assumptions on the hadronisation of charm, in particular on how the quark properties translate into hadron properties. Three examples that are developed in the conceptional design report of the ITS upgrade (ITS-CDR [28]) and shall be shortly summarised here for completeness.

2.4.1 *Non-photonic electron R_{AA} of RHIC*

The non-photonic electron spectrum measured by PHENIX is suppressed for $p_\perp > 2\,\mathrm{GeV/c}$. This could be caused by an Λ_c^+ enhancement and the fact that its branching fraction to electrons is smaller than those of the charmed mesons [40, 41]. The enhancement is further motivated by the observation that the ratio of strange baryons to mesons, Λ/K^0 is indeed enhanced in heavy-ion collisions [42, 43].

Surely, there are many ways to explain an enhancement of an inclusive measurement, but the motivation, the enhancement of Λ/K_S^0, is striking enough to ask for a direct experimental verification.

2.4.2 *Flow of charm*

A very surprising result of ALICE is that there *is* elliptic flow of D mesons in semi-central Pb–Pb collisions [27]. It has been observed earlier that the flow of hadrons scales with their number of constituent quarks [44], which could be well explained by the coalescence model of hadronisation [45]. If this is true, the data shows that charm does not just inherit properties from its initial creation in hard processes, but also interacts significantly enough with the fireball to catch up some collective flow.

Charmed baryons, or multiple charged hadrons would give a unique second handle to further substantiate or to disprove this model.

2.4.3 *Total charm cross-section*

Finally, a precise and, more importantly, model-free measurement of total charm cross-section obviously requires a measurement of the Λ_c^+. Based on the charm fragmentation fractions the Λ_c^+ contribution will be about 7 % to 15 %, i. e. not negligible and with big uncertainty. Moreover, it is completely unclear if the concept of fragmentation fractions makes sense in complicated systems like p–p or even Pb–Pb collisions.

The total charm cross-section is in turn a very important input parameter for many models of charm production in heavy-ion collisions, in particular it is one of the main parameters for thermal models, e. g. [12].

3

Λ_c^+ RECONSTRUCTION IN P–P COLLISIONS

Before going into the complications caused by the large amount of particles emerging from a Pb–Pb collision, this chapter is dedicated to lay out the Λ_c^+ analysis strategy developed in the much cleaner environment of p–p collisions. Emphasis is however put on making the analysis efficient and well suited for the Pb–Pb case. Raw (i. e. uncorrected), $p_\perp$-integrated mass spectra are presented for all decay channels that were discussed in the previous chapter.

3.1 ANALYSIS STRATEGY

From an abstract point of view, the reconstruction strategy applied to the Λ_c^+ case is the same as for all other analyses of short-lived particles: all possible combination of charged tracks of an event, that fulfill the right charge and species combination to form tentative decay products are built, and selection cuts are applied on the accessible variables to increase the statistical significance of the signal. The art, however, is to define these cuts and to apply them in the proper order: cuts do, of course, commute, i. e. the result will not depend on the order of their application—but the time needed to get the result will typically depend dramatically on it.

The choice of the correct strategy is not a completely scientific act, but has much (more than usually acknowledged) to do with aesthetics. This is due to the complexity of the problem and the time it takes to compare different approaches. That said, the remainder of the chapter motivates most of the choices made, but no attempt is made or implied to prove that they are optimal in strict mathematical terms. It will, however, be shown that they are good enough to extract results.

3.1.1 *The ALICE analysis framework*

The data analysis framework employed for the analysis of ALICE's data is based on a hierarchical stepwise approach [46] as follows:

1. The raw detector data ("RAW") is reconstructed into event summary data ("ESD"). In this step the particle tracks are found in all detectors and global tracks are built.

2. The ESDs are filtered and saved in analysis object data ("AOD"). Events are selected based on their trigger class and within events tracks of poor quality are removed.

3. Analysis-specific parameters are calculated and added to the AODs ("delta-AOD"). One example is the search for secondary vertices compatible with the $\Lambda_c^+ \to pK^-\pi^+$ hypothesis.

4. The user analysis code is run on the AOD and/or delta-AOD to carry out the physics analysis (e. g. by filling mass histograms).

The main reason for this procedure is the CPU time necessary to perform each of the steps, which is steeply decreasing from step 1 to 4. What is gained in terms of CPU time has to be traded against flexibility, since any change in an early step of the analysis asks for redoing all subsequent onces.

The analyses presented in this thesis are based on ESDs (i. e. they skip steps 2 and 3). This became possible after a thorough optimisation of the analysis algorithm as explained below.

3.1.2 *Particle identification*

The analysis of Λ_c^+ particles strongly relies on the particle identification (PID) capabilities of the ALICE detector. All the investigated decay modes include a proton, and the three-body decays in addition contain a kaon, which both are much less abundant than pions. Not only does this reduce the computing time, but also does it greatly reduce the background arising from combinations of wrong species.

For this analysis the PID information is then obtained independently from three detectors: ITS, TPC, and TOF. Their information is combined by Baysian inference [47] and a cut on the resulting probability is applied. Each detector assigns a probability vector for the five particle hypotheses (to very good extend only electrons, muons, pions, kaons, and protons are produced/detected, the charge is fixed by the curvature of the track). If sub-detector i assigns probability $p_{k,i}$ to species k, then, according to Bayes law, the probability for the particle to be of species k is:

$$\tilde{p}_k = p_{k,\text{prior}}(p_\perp) \cdot \prod_{i \in \text{detectors}} p_{k,i} \tag{3.1}$$

$$p_k = \frac{\tilde{p}_k}{\sum\limits_{k \in \text{species}} \tilde{p}_k}\,, \tag{3.2}$$

where $p_{k,\text{prior}}$ are the $p_\perp$-dependent prior probabilities.

The priors $p_{k,\text{prior}}(p_\perp)$ are the probabilities that a track with transverse momentum $p_\perp$ is of species k based on the knowledge prior to the measurement. For

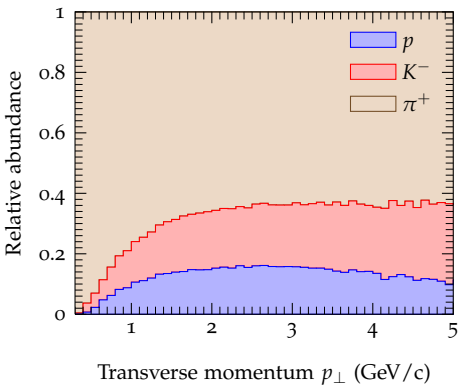

Figure 10: The $p_\perp$-dependent prior probabilities obtained by iteration for $\sqrt{s} = 7$ TeV p–p collisions.

this analysis, the priors are obtained by iteration [48][1]: starting with equal probabilities, $p_{k,\text{prior}}(p_\perp) = 1/5$, tracks are analysed and histograms are filled with the obtained probabilities. Then these histograms are used to evaluate $p_{k,\text{prior}}(p_\perp)$ in the next pass over the data. This procedure eventually converges and the result is depicted in Fig. 10.

3.1.3 *Vertex and particle reconstruction*

Once the particles are identified, all possible combinations that may form a Λ_c^+ decay are analysed separately. From the track parameters of the daughter tracks and the particle species hypothesis, a Λ_c^+ candidate is reconstructed, in particular its kinetic properties (momentum) and its decay point (secondary vertex).

The topological reconstruction method employed here, is the Kalman filter method (a detailed description can be found in [49]). It has several advantages over commonly used methods, with the main ones being speed and correct treatment of error matrices. It builds vertices from tracks in an iterated fashion, such that one may cache the two-particle vertices to reuse them when adding different third tracks.

3.1.4 *Reconstruction algorithm*

A procedure for the analysis of central Pb–Pb collisions has much tighter constrains in terms of computing than any for p–p: with about 100 times more particles produced in the detector acceptance (cf. Sec. 3.3.3), there are potentially 1 000 000 (one million) times more three-body decay candidates to be calculated and analysed.

1 There is no "correct" way to obtain priors, but this is how it is done.

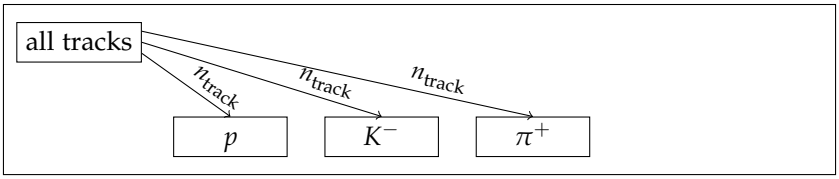

(a) Particle identification ($T_1 = 3n_{\text{track}} \cdot T_{\text{PID}}$).

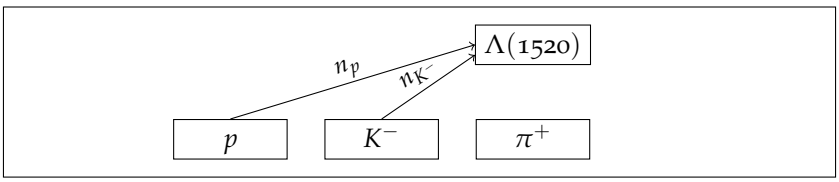

(b) Two-prong (resonance) reconstruction ($T_2 = n_p \cdot n_{K^-} \cdot T_{\text{vtx}}$).

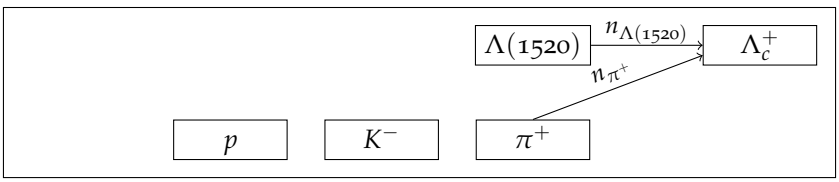

(c) Three-prong (Λ_c^+) reconstruction ($T_3 = n_{\Lambda(1520)} \cdot n_{\pi^+} \cdot T_{\text{vtx}}$).

Figure 11: Sketch of the reconstruction algorithm, here shown for the resonant decay $\Lambda_c^+ \to (\Lambda(1520) \to pK^-)\pi^+$ together with the times needed in each step ($T_{\text{tot}} = T_1 + T_2 + T_3$).

In order to reduce the computing effort, cuts are arranged such that most of the candidates are rejected at a very early stage. The most effective cut in this respect is the particle identification, because amongst the Λ_c^+ decay products there are protons and in case of the three-body decay also a kaon, which are both much less abundant than pions.

The PID, however, is also the most sensitive cut as it relies on a proper calibration of the detector responses, which turned out to be a very delicate business. In the four-step approach outlined the previous section it might therefore be a good idea to trade CPU for more flexibility at a later stage, i. e. to postpone the PID selection to the very end. Unfortunately the additional CPU time could not be afforded in this analysis.

Many of the intermediate quantities needed to build a Λ_c^+ candidate are also used for the calculation of subsequent candidates and a significant speed-up is obtained by proper caching. Examples are the PID calculation as well as the two-particle computation. In the following algorithm these quantities are therefore calculated only once and are then reused.

The algorithm used to analyse the data is sketched in Fig. 11 and works as follows (here for the $\Lambda_c^+ \to pK^-\pi^+$ case, similar for $V^0 + x^+$):

0. Event quality cuts: trigger selection, pile-up rejection.
1. Track cuts: quality and $p_\perp$.
2. Particle identification (Fig. 11a): the tracks are sorted into six sets, one for each polarity and particle species combination (p, $\bar{p}$, K^-, K^+, π^+, π^-); double counting is possible. This is done by requiring a minimal combined, Baysian probability (cf. Sec. 3.1.2) for the particle species hypothesis.
3. Two-particle vertex reconstruction (Fig. 11b): the vertex is built by combining tracks (cf. Sec. 3.1.3) taken from the sets created in the last step. In case of a resonant decay, a mass constraint corresponding to the resonance's mass is applied. The $\chi^2_{\text{red.}}$ of the reconstructed particle/vertex is required to be less than 2.
4. Three-particle vertex reconstruction (Fig. 11c): the vertex is built from the two particle vertex and the remaining particle. The $\chi^2_{\text{red.}}$ of the reconstructed vertex is required to be less than 2.

Here, two- and three-particle vertices are more than just the locations of the decay points, they also contain the kinematic variables. They are thus also called "particles".

Complexity

A main feature of the algorithm is that sets of good and identified particles are created. The loops combining the particles only iterate over their entries, which greatly increases performance.

In terms of execution time, this procedure requires in the case of the inclusive $\Lambda_c^+ \to pK^-\pi^+$ decay: $n_{\text{track}} \cdot T_{\text{PID}} + n_p \cdot n_{K^-} \cdot n_{\pi^+} \cdot T_{\text{vtx}}$, where T_{PID} and T_{vtx} are the times to calculate single PIDs and vertices, respectively. This may be significantly less than $(n_{\text{track}}/2)^3 \cdot (3T_{\text{PID}} + T_{\text{vtx}})$, the running time for first combining all correct charge combinations and doing PID afterwards[2]. In Big Theta[3] notation this is of course the same: $\Theta(n^3_{\text{track}})$. But even in the pessimistic assumption that 30 % of the tracks are identified as protons, 30 % as kaons, and 100 % as pions (double counting is allowed), there is a factor of about eleven between the running time of the two methods.

Speed can directly be translated into physics reach, as this kind of analysis is bound by the available CPU time. To make the problem computable, strong cuts on the single track level are employed to reduce n_{track} before entering the track combination loops. A typical lower cut is the $p_\perp$ of the single track, which renders the reconstruction of Λ_c^+ with low $p_\perp$ impossible. Since Λ_c^+ are likely to be produced mostly at low $p_\perp$ this becomes a crucial issue.

2 One may modify this to $n_{\text{track}} \cdot T_{\text{PID}} + (n_{\text{track}}/2)^3 \cdot T_{\text{vtx}}$ by caching the results of the PID calculation.

3 The "Big Theta" notation is used to characterise the asymptotic behaviour of function: "$\Theta(f(n))$ denotes the set of all $g(n)$ such that there exist positive constants C, C', and n_0 with $Cf(n) \leq g(n) \leq C'f(n)$ for all $n \geq n_0$" [50]

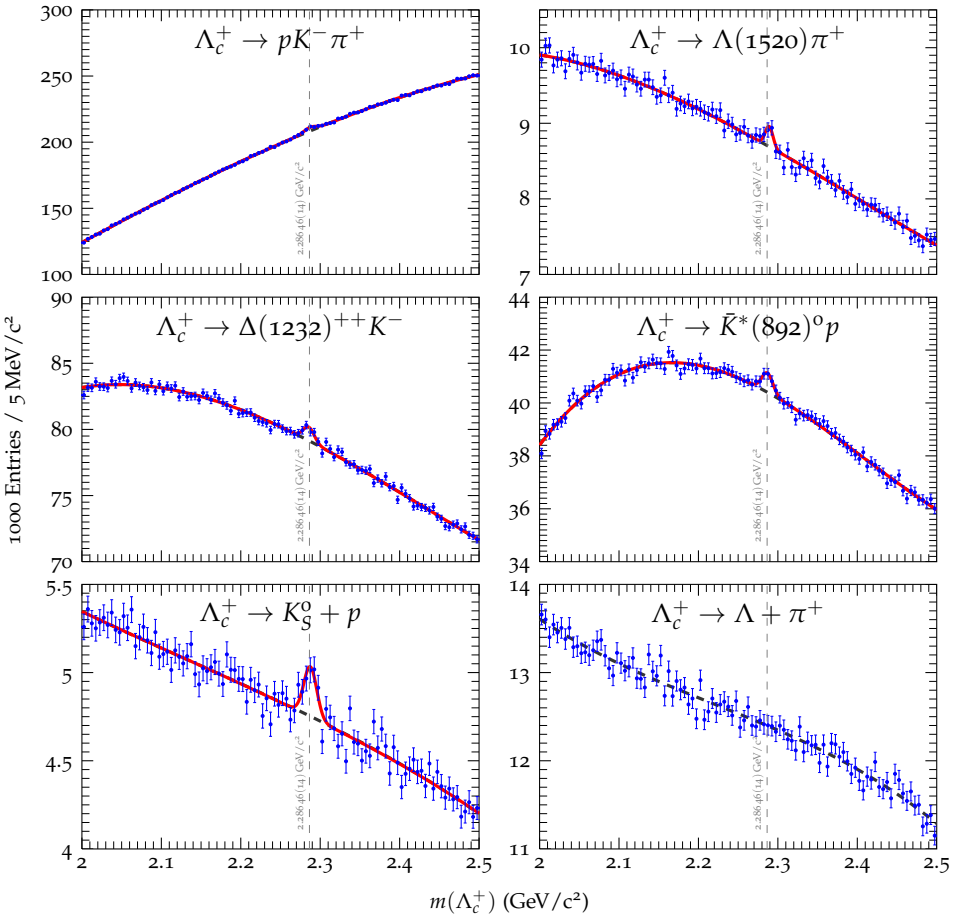

Figure 12: Λ_c^+ mass spectra of different decay channels for $p_\perp^{\Lambda_c^+} > 2.5\,\mathrm{GeV/c}$. The dashed lines show the background fit, while the solid ones are the model function. In the $\Lambda_c^+ \to \Lambda\pi^+$ decay channel no attempt to fit a signal is made as no peak structure is visible (see text for a comment). For extracted parameters see Tab. 3, for a background-subtracted version 13. A similar version of the top four plots appeared as an official ALICE performance figure "ALI-PERF-12817"

3.1.5 *Mass spectra*

After the selection of candidates based on their topology and the particle identification of the daughter tracks, mass histograms are built (Fig. 12 and 13). This is done by combining the four momenta of the three prongs. The number of reconstructed Λ_c^+ is obtained by fitting the spectra to a model function.

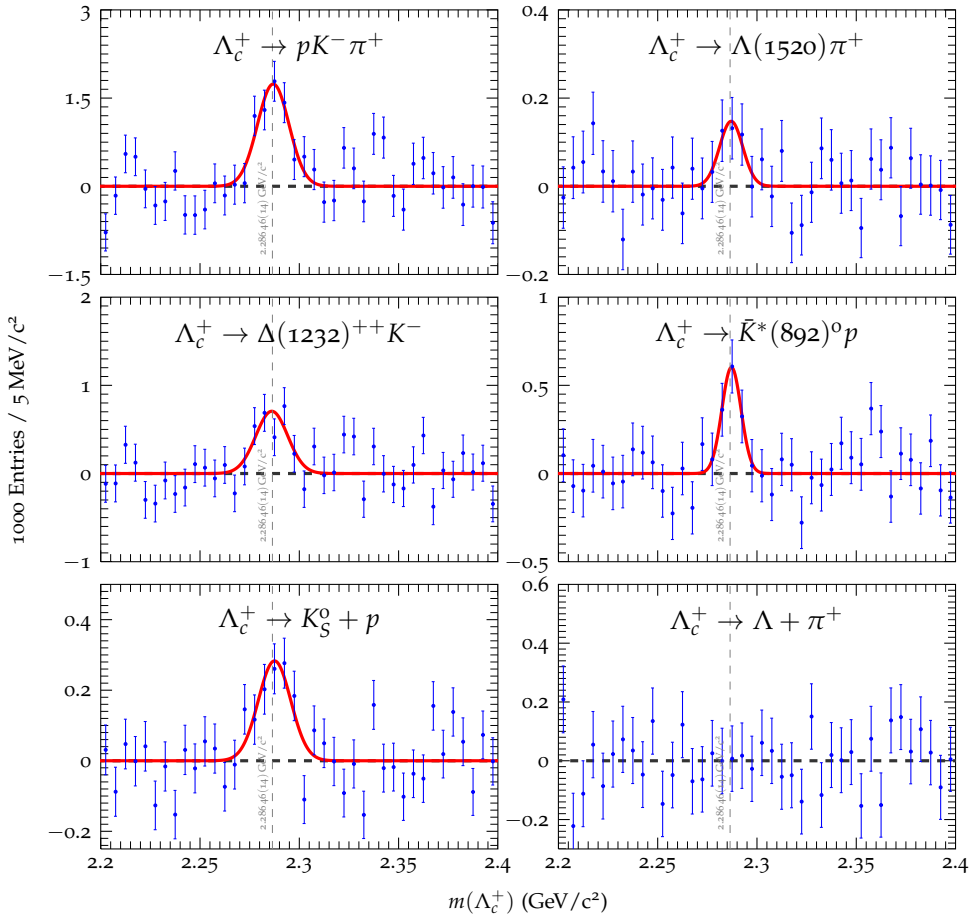

Figure 13: Zoomed and background-subtracted version of Fig. 12.

Fit function

To extract the Λ_c^+ yields from the mass histograms it is assumed that the mass spectrum employs a broad background structure with a narrow peak centered around the nominal Λ_c^+ mass. The two contributions are modeled by a third order polynomial $b(m)$ (parametrised by b_i, $i \in \{0, 1, 2, 3\}$) and a Gaussian peak $s(m)$ (with center μ, width σ, and amplitude $\hat{s}$), respectively:

$$s(m) = \frac{\hat{s}}{\mathrm{erf}(3/\sqrt{2})} \cdot \frac{1}{\sqrt{2\pi\sigma^2}} \exp\left(-\frac{(m-\mu)^2}{2\sigma^2}\right) \tag{3.3}$$

$$b(m) = \sum_{i=0}^{3} b_i L_i\left(\frac{m-\mu}{3\sigma}\right) \tag{3.4}$$

Here L_i are the Legendre Polynomials and erf is the error function[4].

Extracted parameters

The fit has seven free parameters, three for the signal and four for the background part of the model. From the fitted parameters the following three quantities of interest are obtained:

- Signal in $\pm 3\sigma$ (here σ is assumed to be the extracted value from the fit *without* error):

$$S(3\sigma) := \int_{\mu-3\sigma}^{\mu+3\sigma} s(m)\mathrm{d}m = \hat{s} \tag{3.5}$$

- Background in $\pm 3\sigma$ (again no error on σ):

$$B(3\sigma) := \int_{\mu-3\sigma}^{\mu+3\sigma} b(m)\mathrm{d}m = b_0 \tag{3.6}$$

- Significance. It will serve as the figure of merit, quantifying the statistical certainty of the measurement:

$$\mathfrak{S}(3\sigma) := \frac{S(3\sigma)}{\sqrt{S(3\sigma)+B(3\sigma)}} = \frac{\hat{s}}{\sqrt{\hat{s}+b_0}} \tag{3.7}$$

As can be seen from these formulas, the employed parametrisation has the big advantage that the fit will directly yield the quantities of interest and thus its covariance provides the corresponding uncertainties (including the correlation terms).

As auxiliary variables, the position μ and the width σ of the peak are obtained. They are free parameters and give, if found at the nominal Λ_c^+ mass and with a width of about $10\,\mathrm{MeV/c^2}$, further support for a good fit. Here the width is given by the momentum resolution of ALICE and found to be in this region in Monte-Carlo studies of the analysed decays types.

Fitting procedure

In order to make the fitting reliable and to make it applicable in an automated fashion the following method is set up:

1. The mass spectrum is fitted with the background function $b(m)$. For this fit the area of $\pm 30\,\mathrm{MeV/c^2}$ (a bit more than typical values for 3σ) around the nominal Λ_c^+ mass is excluded. This ensures a good first approximation for the background function. Moreover it is a linear fit, such that the global maximum is found and the parameters do not depend on initial values.

4 $L_0(x) = 1$, $L_1(x) = x$, $L_2(x) = \frac{1}{2}(3x^2-1)$, $L_3(x) = \frac{1}{2}(5x^3-3x)$; $\mathrm{erf}(x) = \frac{2}{\sqrt{\pi}}\int_0^x \exp(-x^2)\mathrm{d}x$

2. The fit is repeated with the combined function $f(m) = s(m) + b(m)$, using the nominal mass of the Λ_c^+ and a peak width of $7\,\mathrm{MeV/c^2}$ as initial values.

3. The fit is repeated again, with σ fixed at the value obtained in the previous fit.

The last fit is done for convenience: the quoted $S(3\sigma)$ and particularly the quoted $B(3\sigma)$ and $\mathfrak{S}(3\sigma)$ do—by definition—not include an error caused by the σ uncertainty.

3.1.6 *Summary of cuts*

A number of cuts are applied to enhance the significance of the Λ_c^+. They can be classified as quality cuts and cuts on the properties of the Λ_c^+ candidates.

The first set of cuts, the quality cuts are applied to select only:

- good events: no pile-up. This ensures proper association of track to events.

- good tracks: at least 80 out of possible 159 points in the TPC and at least one point in the two innermost layers of the ITS, as well as a proper track fitting. These tracks will have a good position and momentum resolution, as well as enough PID information.

- good vertices: the $\chi^2_{\mathrm{red.}}$ of the reconstructed vertex shall be less then 2. This removes tracks that are far away from each other, hence unlikely to originate from the same vertex.

The second set of cuts is applied on the kinematic variables of the reconstructed Λ_c^+ candidate as well as on the variables of its prongs:

- The $p_\perp$ of the daughter particles (cf. Fig. 4).

- The distance between primary and secondary vertex ("decay length", $|\vec{l}|$).

- The angle between the decay length and the reconstructed momentum ("pointing angle", $\vartheta_{\mathrm{pointing}}$)

The $p_\perp$ cut is very useful to reduce the combinatorial background due to the soft $p_\perp$ spectrum of produced primary particles. It, however, also has a strong influence on the $p_\perp$ cutoff of the analysable Λ_c^+.

In case of the p–p analyses that are presented here it turned out that the last two cuts are not effective due to the limited detector resolution. They do indeed discriminate the background from the signal but at the same time remove too much signal and thus do not enhance the significance (cf. Eq. (3.7)).

3.2 RESULTS

The analysis chain has been successfully exercised on the p–p data sample of 2010 (see Sec. 1.3.3) and the obtained results are summarised below. It should be emphasised that only uncorrected Λ_c^+ yields are presented. In order to measure the cross-section, acceptance and efficiency corrections need to be computed with a dedicated Monte-Carlo study. In the scope of this thesis, however, the raw yields are the quantities of interest as they better characterise the detector performance and thus benchmark the upgrade.

3.2.1 *Summary*

A summary of the extracted yields, together with their fitted parameters is given in Tab. 3. Due to the lack of an effective selection cut the S/B-ratio is very low. Still, the significances in the inclusive $pK^-\pi^+$ and $K_S^0 p$ channels and the χ^2_{red} values of the background fits are very convincing.

In the $\Lambda_c^+ \to \Lambda\pi^+$ channel no peak was observed. With respect to the $\Lambda_c^+ \to K_S^0 p$ channel, it has a lower branching ratio, a higher background, and comparable acceptance, such that this result is still compatible with the $\Lambda_c^+ \to K_S^0 p$ measurement.

The presented result show the first analyses of the resonant decay channels, as well as of the V^0 modes.

3.3 OUTLOOK

The presented analysis has aimed at showing performance figures of the current detector. While this goal has been achieved, it is of course only the first step in direction of a "physics measurement" like the Λ_c^+/D^+ ratio or the $p_\perp$-dependent Λ_c^+ cross-section. The presented mass spectra have to be corrected for acceptance and reconstruction efficiency and the systematic error sources in the signal extraction have to be addressed quantitatively.

Table 3: Summary of extracted yields in 382 712 096 min. bias $\sqrt{s} = 7\,\text{TeV}$ p–p collisions for $p_\perp^{\Lambda_c^+} \geq 2.5\,\text{GeV/c}$.

channel	μ (GeV/c^2)	σ (MeV/c^2)	$S(3\sigma)$	$B(3\sigma)$	$\mathfrak{S}(3\sigma)$	$\chi^2_{\text{red.,bkg.}}$	$\chi^2_{\text{red.}}$
$pK^-\pi^+$ (incl.)	2.2872(9)	7.65(2)	10 684(1147)	1 912 464(2548)	7.70(83)	1.20	1.17
$\Lambda(1520)\pi^+$	2.2891(24)	4.88(238)	653(183)	50 910(110)	2.87(80)	0.73	0.72
$\Delta(1232)^{++}K^-$	2.2855(18)	7.00	3625(670)	664 683(605)	4.43(82)	1.10	1.09
$\bar{K}^*(892)^0 p$	2.2867(18)	7.00	2549(479)	339 367(375)	4.36(82)	0.87	0.82
$\bar{K}^0 + p$	2.2875(17)	8.15(147)	1153(182)	46 429(119)	5.29(83)	0.95	0.99
$\Lambda + \pi^+$	–	7.00	–	103 652(608)	–	1.06	1.00

3.3.1 *Background treatment*

The absence of a cut that can well seperate signal from background causes a very poor S/B ratio. It is therefore crucial to understand the detailed shape and composition of the background in order to limit the systematical uncertainties of the measurement.

Since no displacement cut is applied in the analysis, the vast majority of the background arises from particles originating from the primary vertex[5]. This indeed is an advantage, as it means that most of the background comes from the combinations of "thermal" primary tracks and, consequently, is smooth.

The way the background is treated or "removed" in this analysis, is by fitting *some* model function, $b(m)$, to the data assuming that the background is reasonable smooth. This function is then subtracted from the mass spectrum (from Fig. 12 to Fig. 13).

This procedure introduces some hard to control systematic error, because the choice of $b(m)$ is arbitrary. The only constraint is that the χ^2_{red} value for its fit in the (assumed to be peak-free) sidebands around the peak is close to 1.

In the future, in particular in Pb–Pb, data-driven methods can be employed to reduce the systematic uncertainties due to the background treatment. Event mixing looks very promising in this respect (though one has to be careful due to the resonant decay structure) and is currently investigated.

3.3.2 *Physics measurements*

With precise mass spectra the road to a cross-section measurement is paved. Indeed the large number (over ten thousand) of $\Lambda_c^+ \to pK^-\pi^+$ decays makes it possible to extract a $p_\perp$-differential cross-section in at least three $p_\perp$ bins. Moreover, the presented two classes of decay channels are a very useful cross-check as they suffer from different systematic errors. Moreover do the V^0 channels allow to probe the low-$p_\perp$ part of the Λ_c^+ spectrum since they do not suffer as much from the high combinatorial background from low-$p_\perp$ primary tracks.

3.3.3 *Extrapolation to Pb–Pb*

The raw mass spectra obtained from 382 712 096 p–p events clearly demonstrate nice performance of the detector. While the measurements of the $p_\perp$-differential Λ_c^+ cross-section and the Λ_c^+/D^+ ratios are well advancing, no trace of signal has been observed so far in Pb–Pb collisions. In this section the reasons are laid out.

5 In case of the $V^0 + x^+$ cases, this concerns the bachelor only. The V^0 candidates have much better purities.

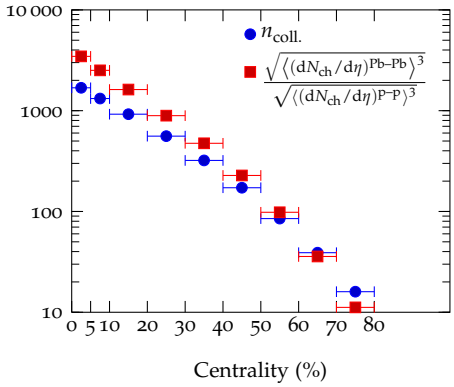

Figure 14: Scaling of signal S (proportional to the number of binary collisions, $S \propto n_{\text{coll.}}$) and square root of background $\sqrt{B}$ (the background scales as $B \propto \langle \mathrm{d}N_{\text{ch}}/\mathrm{d}\eta \rangle^3$, see text for comments) with centrality. The numbers are from [51] and [26].

Scaling of signal and background

If there were no effects due to the media and high particle densities, the amount of Λ_c^+ created in a Pb–Pb collision should scale proportionally to the number binary collisions. This number can be calculated using the Glauber model [11] (Fig. 14).

The background scales proportional to the number of produced particles to the third power, as all analysed channels have a three-particle final state. This is a very unfortunate situation, since the multiplicity rises much faster than the signal, leading to a worsened S/B ratio (Fig. 15a). The relevant number for the analysis is however the fluctuation of the background, i. e. the square root of possible Λ_c^+ candidates, such that the relevant number is $\sqrt{n_{\text{track}}^3}$ (Fig. 14).

Combined, what really matters is the significance $\mathfrak{S}$ of the signal, for a given number of events, which is shown in Fig. 15b. It shall be noted, that this figure only holds if the number of events in a centrality bin equals the number of p–p events.

Scaling of running time

Another complication is the number of collisions collected in Pb–Pb as compared to p–p. Not only is the LHC time dedicated to Pb–Pb much shorter (one month per year) than that used for p–p (eight months per year), but also is the trigger rate that can be handled by the experiment much smaller in the Pb–Pb case due to the larger event sizes[6]. Moreover, Pb–Pb collisions introduce another variable, the centrality, that one needs to take into account. If one is for example interested

6 The LHC also provides lower collision rates, but they are still higher than what can be digested by ALICE, see Chap. 5

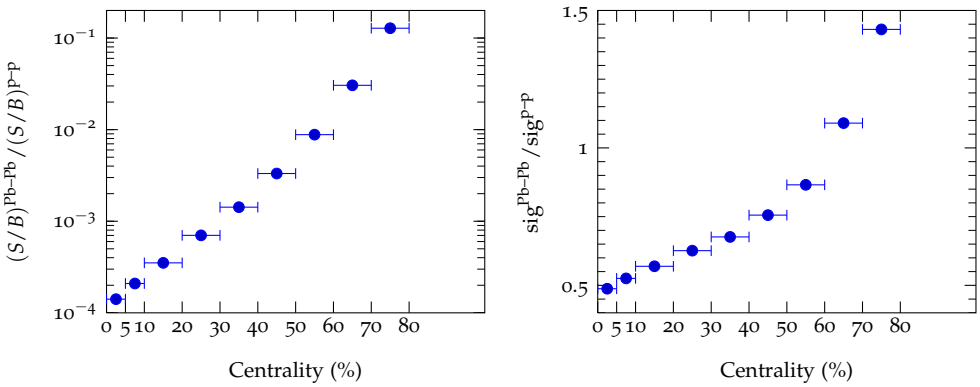

(a) Scaling of signal to background, S/B, ratios.

(b) Scaling of significance $\mathfrak{S}$

Figure 15: Scaling for $\sqrt{s_{NN}} = 2.76\,\text{ATeV}$ Pb–Pb wrt. $\sqrt{s} = 7\,\text{TeV}$ p–p. Same settings as for Fig. 14

in the 5 % most central collisions, but the experiment is recording minimum bias data, one needs 20 times the statistics.

4

ITS UPGRADE

The last chapter has revealed the difficulties of the analysis of the Λ_c^+ decays in p–p collisions—and its hopelessness in central Pb–Pb collisions. In particular it was shown that the most important cut variable, the decay length, as successfully used in the analysis of the charmed mesons [14, 52] is not accessible in the analysis of the Λ_c^+ because of its too short decay length. In this chapter it will be demonstrated that with a new inner tracking system (ITS) made of cutting edge technology, resolutions may be achieved, which allow to employ this cut. This is turn is shown to render the $\Lambda_c^+ \to pK^-\pi^+$ channel accessible over a wide $p_\perp$ range even in central Pb–Pb collisions.

4.1 THE CURRENT ITS

A short overview of the relevant ITS parameters for the analysis of short-lived particles is given here. For a detailed detector description it shall be referred to [20, 53].

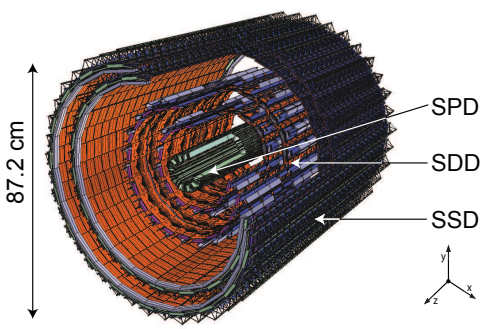

Figure 16: The layout of the current ITS. Figure taken from [53].

4.1.1 *Layout*

The currently installed ITS of ALICE is made of six layers of silicon detectors (Fig. 16. Different technologies are used from the inner- to the outer-most layer: two pixel, two drift, and two strip detectors. They are characterised by different resolutions, summarised in Tab. 4. Together with the thickness of the beam pipe ($X/X_0 \approx 0.22\,\%$ [28]) they determine the track position resolution. Here the resolution is quoted in the $r\phi$- and z-directions, the two parameters which span the plane that is perpendicular to the track direction at the collision point.

The current tracking strategy of ALICE tracks from "outside to inside": tracks are found in the TPC and then prolonged through the ITS and finally extrapolated to the collision point. Based on this strategy the optimum positions and types of detectors of the ITS were determined.

4.1.2 *Performance*

The track resolution provided the current ITS is of the order of 100 µm [53]. It has been proven to be crucial for the analysis of charmed mesons. Owing decay lengths of a few 100 µm their secondary vertices could be well resolved and thus background from the primary vertex could be strongly suppressed, both in p–p [52] and Pb–Pb [14] collisions.

As already stated the requirements for the Λ_c^+ are stronger due to its short decay length of only 59.9 µm.

4.2 UPGRADE PROPOSAL

The ALICE collaboration has decided to pursue the study of possible detector upgrades for the era of operation after the planned long shut down of LHC in 2017–2018. In this course a conceptional design report (CDR [28]) for a new inner tracker system has been devised. The analysis of the Λ_c^+ particle, as laid out here, has become one of the main physics performance benchmarks.

Table 4: Properties of the current ITS layers [53].

Layer	Technology	Radial position (cm)	Resolution (µm) $r\phi$	Resolution (µm) z	radiation length (%)
1	pixel	3.9	12	100	1.14
2		7.6			1.14
3	drift	15.0	35	25	1.13
4		23.9			1.26
5	strip	38.0	20	830	0.83
6		43.0			0.86

4.2.1 *Layout & technology*

The precise layout of the upgrade has not yet been decided on. However, it is certain that it will be lighter in terms of radiation length and will use detector elements with higher precision. Also will it be placed more closely to the interaction point. Possibly, the beam pipe will be replaced by a thinner one.

From the analysis point of view, the precise layout does not matter too much, but rather are the resulting track resolutions and the tracking efficiency of importance. While as the latter does influence the performance of the analysis in a rather straight forward manner, the impact of improved track resolutions has a less obvious influence and needs careful study.

For the sake of the further analysis three models are considered. They consist of seven layers and are distinguished named by their radiation length per layer: 0.1 %, 0.3 %, and 0.5 % (details in [28]). The most likely scenario is the middle one, and the others serve as a check to see the trend when changing the material budget.

4.3 SIMULATION

In order to assess the performance of a possible upgrade, dedicated Monte-Carlo studies were carried out. The are based on the existing ALICE Monte-Carlo, both for the sake direct comparability to the current set-up and the time needed to perform such a comparison. At some point, when the detector requirements are better understood a detailed and dedicated Monte-Carlo is of course unavoidable. Till that point is reached, however, fast tools allow much better insight.

4.3.1 *Pointing resolution*

The basic ingredient for the simulations is the pointing resolution of the tracks. "Pointing resolution" refers to the spatial resolution of tracks in the vicinity of the collision point. It is also the main quantity that will help the analysis of short-lived particles such as the Λ_c^+ as it will eventually allow to distinguish their decay vertices form the main collision vertex.

The pointing resolution is determined by the position of the detector elements as well as their resolutions and material budget. The latter causes multiple scattering and thus worsens the resolution. In this regard also passive elements like the beam pipe and air have to be considered. Given a detector layout, the resolutions can be estimated quite accurately by a simple error propagation formula, known as the telescope equation [54]. The results are shown in Fig. 17 for different upgrade scenarios.

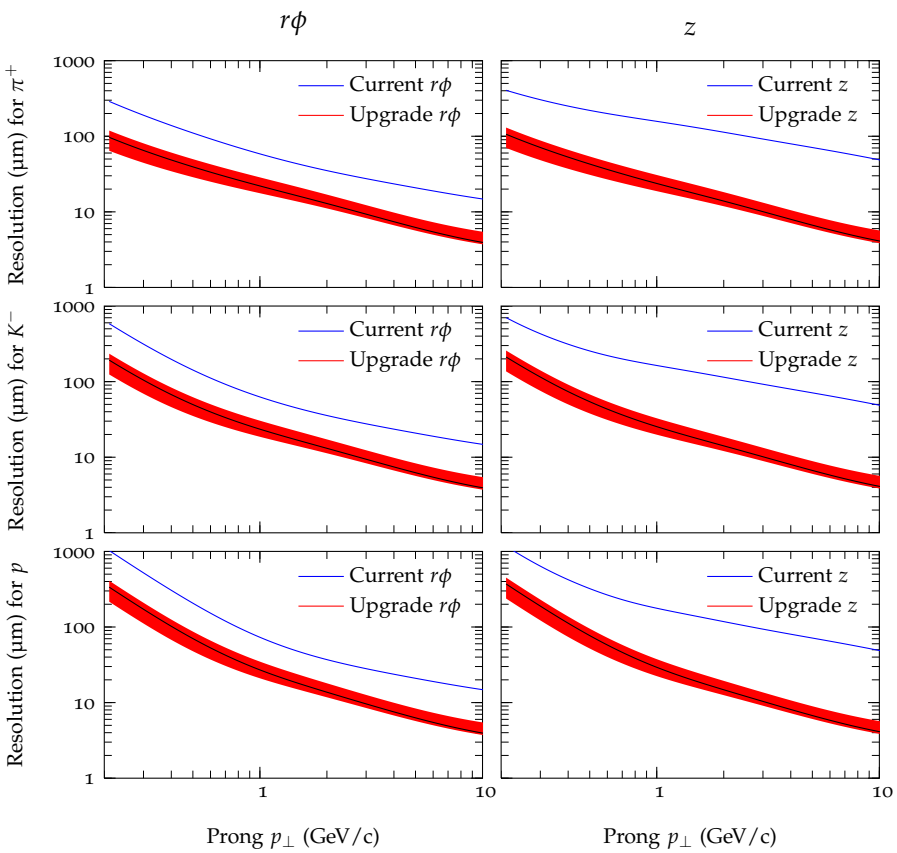

Figure 17: Simulated pointing resolutions in $r\phi$ and r directions for three different particle species (the prongs of $\Lambda_c^+ \to pK^-\pi^+$) in the current and the upgraded scenario. The shaded bands indicate by how much the resolution changes when varying the nominal upgrade setting ("0.3 %") to the 0.1 % or 0.5 % settings.

4.3.2 *Monte-Carlo data set*

A data set with 10 000 central Pb–Pb events at $\sqrt{s_{NN}} = 5.5$ ATeV, the nominal collision energy foreseen, was created using the HIJING [36] event generator. On top a number of Λ_c^+ particles were added to each event. These were forced to decay into the golden decay modes that were discussed in the previous chapters. In addition it was required that all prongs of the three-prong decay are within $|\eta| < 0.9$ to increase their chances to be reconstructed.

The introduced enhancement of signal was corrected using a minimum bias Monte-Carlo simulation and found to be roughly a factor of 340, such that the analysis is also speeded up by this factor. Care had to be taken of the different

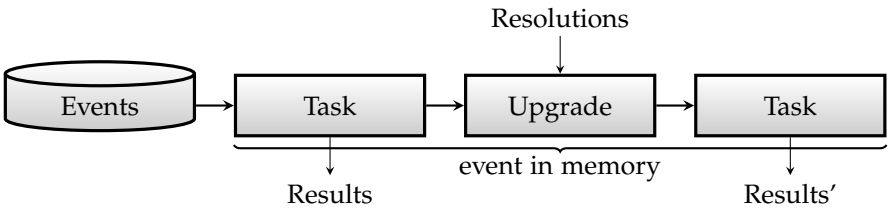

Figure 18: Schematic picture of the data flow of the "hybrid" simulation approach. The analysis is run twice: First it is run with the Monte-Carlo of the current detector. Then the resolutions of the reconstructed tracks are improved using the Monte-Carlo information. Finally the same analysis is run again.

background sources that do only appear because of the Monte-Carlo addition like for example background from two different Λ_c^+ decays. These contributions have been removed from the extracted mass spectra.

4.3.3 *Application of resolution improvements*

Since the detailed simulation of a given detector layout is very time consuming (order of months for each "detector idea"), a faster approach was followed: the pointing resolutions of the new detector were simulated as explained above and the existing Monte-Carlo for the current detector was retrofitted to the new resolutions. This was done by altering the track parameters such that their error with respect to the Monte-Carlo truth is reduced by a factor that corresponds to the improvement of impact parameter resolution as predicted for the new set-up (Sec. 4.3.1). That is[1]:

$$\begin{pmatrix} y \\ z \\ \sin\phi \\ \tan\theta \\ 1/p_\perp \end{pmatrix}' = \begin{pmatrix} y_{\mathrm{MC}} + \sigma^{\mathrm{new}}_{d_{o,r\phi}}(p_\perp)/\sigma^{\mathrm{old}}_{d_{o,r\phi}}(p_\perp) \cdot (y - y_{\mathrm{MC}}) \\ z_{\mathrm{MC}} + \sigma^{\mathrm{new}}_{d_{o,z}}(p_\perp)/\sigma^{\mathrm{old}}_{d_{o,z}}(p_\perp) \cdot (z - z_{\mathrm{MC}}) \\ \sin\phi \\ \tan\theta \\ (1/p_\perp)_{\mathrm{MC}} + \sigma^{\mathrm{new}}_{1/p_\perp}(p_\perp)/\sigma^{\mathrm{old}}_{1/p_\perp}(p_\perp) \cdot ((1/p_\perp) - (1/p_\perp)_{\mathrm{MC}}) \end{pmatrix}. \tag{4.1}$$

As can be seen from the formula also the $p_\perp$ resolution improves, which however does not play an important role in the case that the TPC is present.

The analyses are then carried out with the "normal" resolutions and again with the altered resolutions, such that the effect of the upgrade becomes visible. This is depicted schematically in Fig. 18.

Similarly to the track parameters the associated covariance matrix is scaled. This in particular means that the χ^2 value associated to a real Λ_c^+ vertex, which is one of

1 For a description of the tracking see [24].

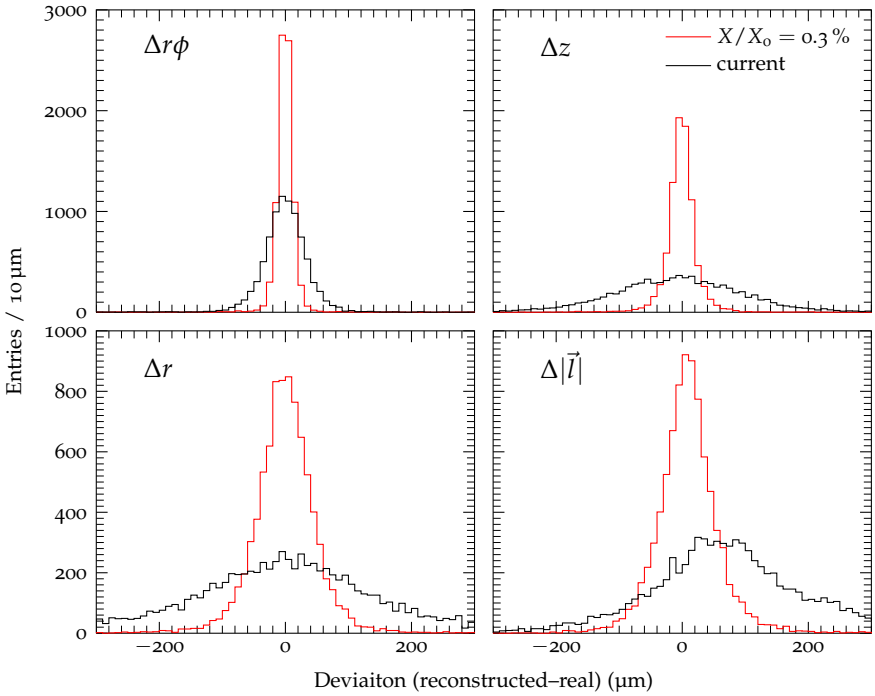

Figure 19: The resolution of the secondary vertex position for the current ITS and the nominal ("$X/X_0 = 0.3\,\%$") upgrade proposal. Here shown in the local Cartesian system (with directions r, $r\phi$, and z) as defined by the momentum of the Λ_c^+ in cylindrical coordinates. Also shown is the difference of reconstructed decay length and real decay length (in three dimensions), $\Delta|\vec{l}|$. All settings are for the Λ_c^+ $p_\perp$ bin of 4 GeV/c to 6 GeV/c.

the main cut variables, will not change—but the χ^2 of the background candidates will become much larger.

4.3.4 *Secondary vertex resolution*

The resolution of the secondary vertex is a function of Λ_c^+ decay topology and the single track resolutions of the prongs. The two have to be "convoluted" and the result is shown in Fig. 19 for the standard upgrade scenario. It can be clearly seen that the resolution of the most important quantity, the distance between primary and secondary vertices, $|\vec{l}|$, improves significantly and—most importantly—becomes smaller than the typical decay lengths of the Λ_c^+. Thus, it will give a new handle to remove majority of the combinatorial background originating from the primary vertex.

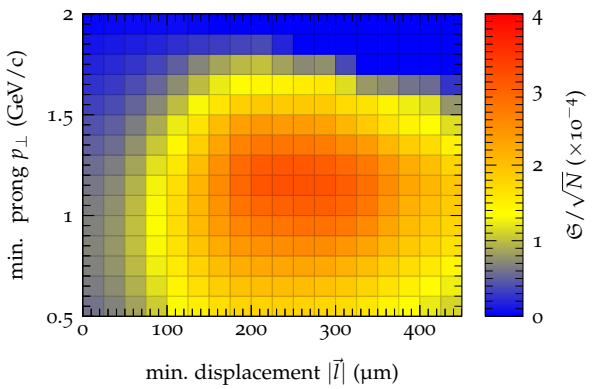

Figure 20: An example dependence of the significance $\mathfrak{S}$ on the two major cuts as it is used for the cut optimisation procedure (here for $p_\perp^{\Lambda_c^+} \in [4,6)$ GeV/c and the nominal, "$X/X_0 = 0.3\,\%$", upgrade scenario).

4.4 IMPACT ON THE $\Lambda_c^+ \to pK^-\pi^+$ ANALYSIS

To address the impact of the upgrade quantitatively the $\Lambda_c^+ \to pK^-\pi^+$ analysis, as laid out in Chap. 3, is carried out for the different settings. To obtain comparable results, the analysis cuts are automatically readjusted for the different detector layouts.

4.4.1 *Cut optimisation*

It was already mentioned in Chap. 3 that the choice of cut variables contains some arbitrariness. Once this choice has been made, one can however optimise the cut *values*. This is a n-dimensional minimisation problem and was carried out here for the two-dimensional, $p_\perp^{\text{prong}} \times |\vec{l}|$, subspace. For different combinations the significance $\mathfrak{S}$ is computed and a clear maximum appears (Fig. 20).

The significance is of course not the whole story. Each cut value yields a certain number of signal per event, S/N, and certain number of background candidates per event, B/N. This corresponds to a point in a S/N–B/N space, which resembles a phase diagram. By a (non-linear) co-ordinate transformation the $\mathfrak{S}/\sqrt{N}$–S/B plot is obtained. This is shown for different detector configurations in Fig. 21. Important is to remark that here the point that maximises the significance $\mathfrak{S}$ defines the optimum. One could well argue to better trade a bit of significance for a better S/B and Fig. 21 shows the available choices.

The maximisation procedure was carried out for all $p_\perp$ bins and detector configurations independently and the values of significance and S/B at the point of maximum significance are plotted in Fig. 22.

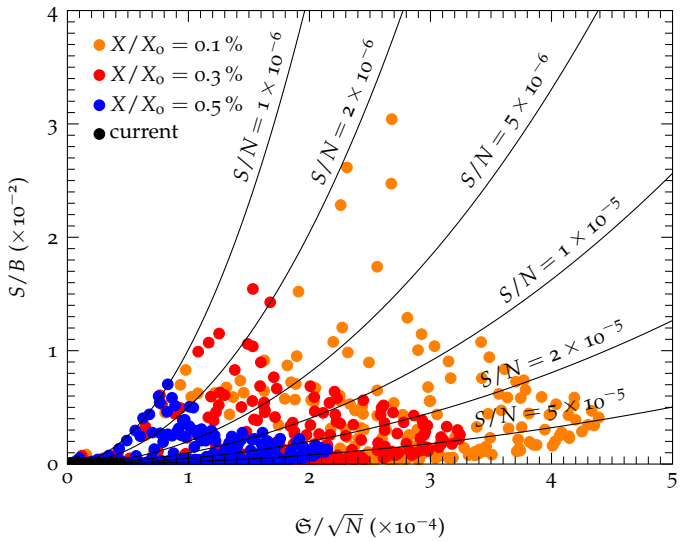

Figure 21: An example cut phase diagram for different upgrade scenarios for $p_{\perp}^{\Lambda_c^+} \in [4,6)$ GeV/c bin. The points correspond to different choices of the cuts as that are indicated in Fig. 20.

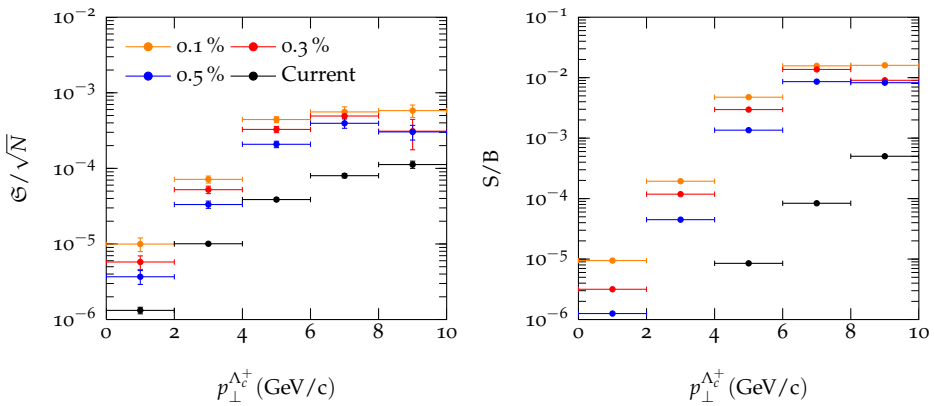

Figure 22: The obtainable maximum significances and the *corresponding* signal to background ratios.

4.5 SUMMARY

The analysis of the Λ_c^+ has been shown (Fig. 22) to strongly benefit from an ITS upgrade over the whole momentum range. The significances improve by factors of 7 to 10, which would correspond to a "speed-up" of 50 to 100 if one naively translates it to running times.

While as the obtainable significances with 10^9 events are still rather low, or only possible at higher transverse momenta, they are surely too low in case of the current detector. With an improved read-out network, up to 10^{10} events will be recordable which renders the analysis feasible for a wide momentum range [29, 28].

5

TPC UPGRADE

The previous chapter has reveiled that the resolution of the current ALICE detector imposes a limitation on the analysis of the Λ_c^+ (amongst others). But besides the resolution there is a second limitation especially relevant for rare processes: the number of recorded events, or the maximum event rate. In ALICE this rate is limited by the TPC, which is the slowest sub-detector—LHC would already now be able to provide interactions at much higher rates, esp. in case of p–p collisions and plans are to further increase the luminosity (also for Pb–Pb) in the upcoming years.

In this chapter the limiting factors for the TPC read-out rates are analysed and on that basis a possible cure—a new read-out network—is proposed. A demonstrator circuit of the main part of this new network is developed. Together with a detailed read-out simulation it proves the feasibility of such an upgrade and quantifies the possible speed-up: more than a factor of ten.

5.1 THE CURRENT TPC

In the following a short summary of the most relevant aspects of TPCs in general and that of the ALICE TPC in particular is given. Albeit being conceptionally very simple detectors, the realisations become very involved: the commissioning, calibration and operation of the ALICE TPC is part of many PhD theses (e. g. [55, 56, 57, 58]), and the detector is still the source of interesting detector-physical effects (e. g. [59, 60] or [61]). Thus, a thorough documentation of the detector itself is clearly out of scope and it shall be referred to its design report [21] and to a more recent review [18].

5.1.1 *Working principle*

TPCs are gaseous detectors for tracking and particle identification (see e. g. [62] for a good introduction). They employ a gas volume in which ionisation is used as the detection mechanism: charged particles crossing the gas produce charged tracks along their trajectories. The energy depositions is described by the "Bethe-Bloch formula" and is dependent on the particles' charge, mass, and momentum. There-

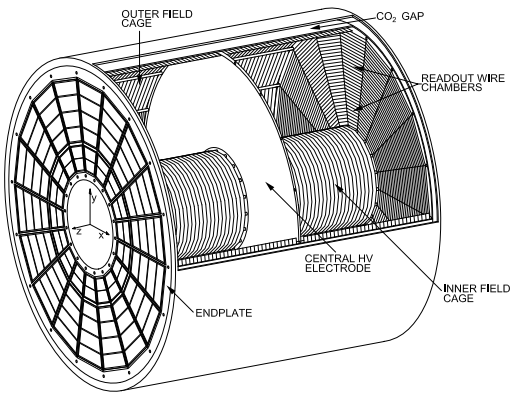

Figure 23: Schematic drawing of the TPC. The size of the dector is roughly 5 m × 5 m (diameter × length). Figure taken from [18].

fore the resulting ionisation paths do not only picture the particles' trajectories but on top does the amount of ionisation contain information about the particles' species.

An electric field is applied to make the electrons that were liberated in these ionisations drift towards read-out chambers where they are amplified and their arrival time and position as well as their charge density are recorded. Together with the interaction time, the position of the creation of the incoming electrons can be calculated by reversing their drift path, which finally yields the full collision geometry.

5.1.2 *Layout*

The TPC used in ALICE is built as a hollow cylinder placed concentrically around the beam line and is read out at the end-plates. It has dimensions (in terms of active volume) of $85 < r < 247$ cm in radial, and $|z| < 250$ cm in beam-direction. Its gas volume is divided into half by a central electrode, which is held at a negative potential (-100 kV) such that the electrons drift along straight lines with constant velocity[1] towards the two end-plates where they are amplified and recorded. The amplification is performed by one of 72 read-out chambers. The end-pates are divided into 18 sectors with each containing an inner and an outer read-out chamber (IROC and OROC). The chambers are realised as gated multi-wire proportional chambers (MWPCs) and provide the necessary gas amplification with a gain factor of 3000 to 6000. Read-out is performed using cathode pads: the cathode plane is divided into a total of 557 568 pads with pad sizes of (inner to outer) $4 \times 7.5\,\text{mm}^2$,

1 The electron drift is governed by the "Langevin equation". Deviations from a straight line of the order of 1 cm are measured in ALICE and can be attributed to electric and magnetic field inhomogeneities. See [56, 63, 64, 65] for details.

$6 \times 10\,\mathrm{mm}^2$, and $8 \times 15\,\mathrm{mm}^2$, taking into account the higher track density at smaller radii.

The gating of the MWPCs (a layer of wires) can isolate the detection volume from the amplification region, by changing the electrostatic field configuration at the entrance of the chambers[2]. Electrons that are produced by primary ionisation are intercepted before they can produce an avalanche in a chamber. This avoids space charge and the resulting gain variations in the ROCs and also reduces their aging. But, more importantly, gas ions that are produced in an avalanche are caught before leaking out into the field cage (where they would distort the electric field). To achieve the optimal performance, the gating is only opened when an event is acquired. Afterwards it stays closed for at least 180 µs, until all avalanche ions are intercepted [56].

5.1.3 *Read-out electronics*

In terms of read-out electronics, the TPC is made of 557 568 active channels—one for each pad—that are read out completely in parallel. The resulting channel density could only be achieved by using custom build electronics and placing the full signal processing (amplification, shaping, digitisation, post-processing, and buffering) on-detector.

Placing electronics on-detector has important implications: is has to work in magnetic field (0.5 T) and under radiation[3] (see [67] for an estimation of doses and fluxes).

PASA and ALTRO

In order to achieve the required level of integration, a pair of ASICs, called PASA ("pre-amplifier shaper" [68]) and ALTRO ("ALICE TPC read-out chip" [69]) was designed. The PASA is made of a charge-sensitive amplifier and an analog shaper, while the ALTRO digitises the signal and post-processes it. Both chips comprise 16 independent channels.

The digitisation of the signal is performed at 10 MSPS with a resolution of 10 bit, yielding a total data volume of about 700 MByte (assuming an acquisition time of 100 µs). In order to reduce the data volume, zero-suppression is employed and only samples above a certain threshold are stored[4]. The formatting of the resulting data stream is done using run-length encoding, such that the resulting event sizes depend on the number of samples above threshold and their distribution (given by the event topology).

2 This is a delicate operation and has a subtle side effect: [59, 60].

3 LHC induced radiation effects (single event upsets) have been measured within the ALICE TPC electronics: details in [61, 66].

4 The actually implemented circuit is a bit more complex [69] but for all further considerations this does not matter.

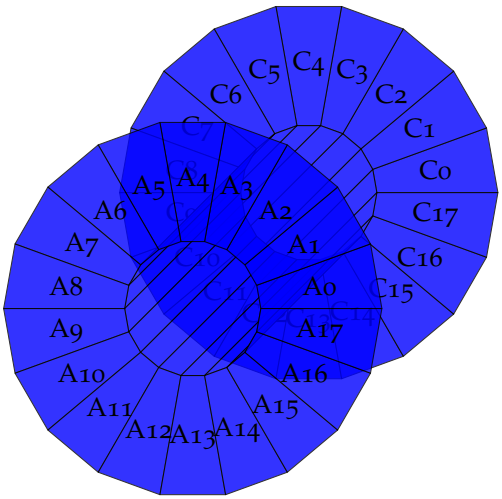

(a) Sectors of the TPC.

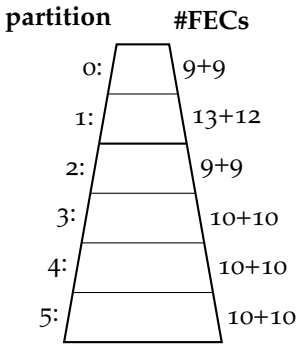

(b) The distribution of FECs onto partitions within each sector.

Figure 24: The distribution of electronics over the TPC end-plates. Note the inhomogeneous distribution of FECs (in particular the "excess" in partition 1) due to the different pad and area sizes covered by the partitions.

In addition the ALTRO contains a multiple-event memory, that allows to buffer up to four complete events. It decouples the acquisition from the read-out, which can greatly reduce the dead time (details in Sec. 5.3.3).

FECs

Eight pairs of ALTRO and PASA are mounted together on one of 4356 front-end cards (FECs), the smallest units of the read-out system in terms of PCBs. In addition to the ALTROs and PASAs, FECs also have some local intelligence, realised by an FPGA ("board controller", BC) that is used to monitor voltages, currents and the local temperature. Is is also able to switch on and off local voltage regulators to avoid damages if the system malfunctions (e. g. because of radiation). Moreover, the BC can also talk to the ALTROs, which is used to implement a special read-out mode "sparse read-out", which is of particular use for p–p data taking, where track density is so low that the detector is essentially empty (details in [58, 70]).

The 4356 FECs are distributed over the TPC end-plates, grouped into 216 "read-out partitions" (see Fig. 24). Within a partition they are connected to a parallel bus. It is made of 40 data and 15 control and clock signals[5] (see Tab. 5), of which

5 The only signal, which is separately routed to each FEC is the `cardsw`-signal, which is used to turn on and off the cards.

Table 5: The digital interface of the FEC.

name	type	#lines	direction	comment
`data[39:0]`	GTL	40	FEC $\leftrightarrow$ RCU	data/address
`error`	GTL	1	FEC $\rightarrow$ RCU	
`dstb`	GTL	1	FEC $\rightarrow$ RCU	data strobe
`ackn`	GTL	1	FEC $\rightarrow$ RCU	acknowledge
`trsf`	GTL	1	FEC $\rightarrow$ RCU	transfer
`l1`	GTL	1	FEC $\leftarrow$ RCU	L1 trigger
`l2`	GTL	1	FEC $\leftarrow$ RCU	L2 trigger
`write`	GTL	1	FEC $\leftarrow$ RCU	write enable
`cstb`	GTL	1	FEC $\leftarrow$ RCU	command strobe
`rst`	GTL	1	FEC $\leftarrow$ RCU	reset
`scint`	GTL	1	FEC $\rightarrow$ RCU	slow control interrupt
`scdin`	GTL	1	FEC $\rightarrow$ RCU	slow control data
`scdout`	GTL	1	FEC $\leftarrow$ RCU	slow control data
`scclk`	GTL	1	FEC $\leftarrow$ RCU	slow control clock
`cardsw`	open drain	1	FEC $\leftarrow$ RCU	card switch
`rclk`	GTL	1	FEC $\leftarrow$ RCU	read-out clock
`sclk`	P-ECL	2	FEC $\leftarrow$ RCU	sampling clock

most are implemented as GTL[6]. The bus runs at a frequency of $f_{\texttt{rclk}} = 40\,\text{MHz}$, yielding a peak bandwidth of 200 MByte/s.

RCU

Within a partition the bus connects the FECs to a read-out control unit (RCU). More precisely, each RCU has two buses ("branch A" and "branch B"), each connected to half of the FECs (one more FEC on branch A in case of partition 1). Having two busses helps to reduce the overhead imposed by the used bus protocol (details in Sec. 5.3).

On the other end the RCU implements the interface to the off-detector systems, which comprise:

- Data acquisition (DAQ); via a custom-made optical link ("detector data link", DDL) with a bandwidth of 160 MByte/s. [71]
- Trigger; via another custom-made optical link that provides also the LHC clock signal. [72]
- Detector control system (DCS); via a modified version of 10 Mbit/s Ethernet. [73, 74]

6 "Gunning transistor logic"—a digital signaling standard named after William Gunning.

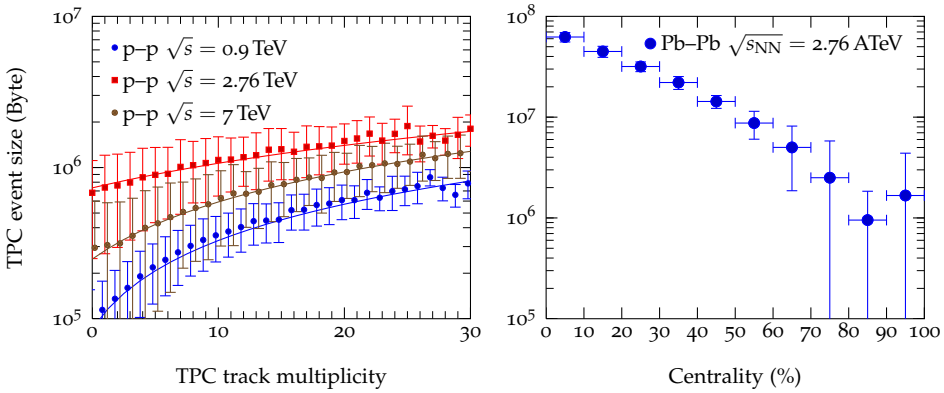

Figure 25: The event size of the TPC in dependence of the event multiplicity (p–p) or centrality (Pb–Pb) for different energy/beam settings. The error bars depict the event to event fluctuations. Solid lines (left plot only) are affine fits of the size to the number of tracks (see text for details).

5.2 EVENT SIZES

The first parameter that is important for the architecture of the read-out network is the data size of an event. As mentioned above the ALTRO chips perform zero-suppression to compress the data. This leads to an event size that varies with the number of samples above threshold and their distribution. In this section this generic statement is exploited in terms of physics observables.

5.2.1 *Event-Topology dependence*

The relevant physical quantities, in which the event size dependence shall be studied, are track multiplicity[7] or—more appropriate for Pb–Pb—collision centrality. The resulting dependencies are shown in Fig. 25.

If only a small number of tracks, n_{track}, is produced then these are independent, i. e. separated well in space and one expects the event size, s, to depend linearly on it:

$$s(n_{\text{track}}) = s_0 + \alpha \cdot n_{\text{track}} \,. \tag{5.1}$$

The solid lines in Fig. 25 (p–p) show a fit to this model. The results are $\alpha = 24(2)$, $33(9)$, and $34(7)$ kByte/track for $\sqrt{s} = 0.9$, 2.76, and 7 TeV, resp. If the track multiplicity raises this approximation becomes worse as tracks start to overlap, which causes the data volume to grow sub-linear. In addition to the scaling with the number of tracks, there is some offset, s_0, in the event size that is caused

7 Herein a "track" is a measured quantity that is required to fulfill certain quality criteria. In particular it has to be within $|\eta| < 0.8$.

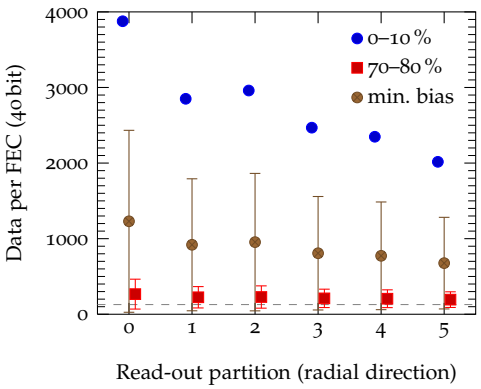

Figure 26: Event sizes per partition for $\sqrt{s_{NN}} = 2.76$ ATeV Pb–Pb events in terms of 40 bit words as they are transferred on the FEC bus. The numbers are normalised to a FEC (which varies with partition; see Fig. 24). The dashed line indicates the minimum (128 trailer words).

a) by the data formatting, and b) by some background signals. Sources for the latter are noisy channels as well as particles that are produced far away from the interaction. The latter fly parallel to the beam line and are not counted as "tracks" (in the transverse plane they look like points or small circles). The different offset values are due to different running conditions and can be attributed to different LHC induced backgrounds.

While the considerations above concern the *mean* event size, one observes a big event-by-event fluctuation (depicted by the "error bars" in Fig. 25). This is because different kinds of tracks (e. g. different specific energy losses, inclinations, and/or bending radii) cause different data volumes and because the overlapping regions of tracks fluctuate as well.

Further on it is solely dealt with the Pb–Pb case.

5.2.2 *Data distribution*

At least equally important as the total size of an event is how it is distributed over the detector in space. Being azimuthal symmetric, the important dependence is radial. The event size per FEC (128 channels) is shown in dependence of the read-out partition for central and min. bias $\sqrt{s_{NN}} = 2.76$ ATeV Pb–Pb events in Fig. 26. With regard to Fig. 24 one should notice that the data volume per RCU has to be multiplied by the respective numbers of FECs[8].

The event-size also depends on the event type (e. g. its centrality) and thus varies with time. Moreover the distribution of data in space need not be isotropic for a *given* event (e. g. due to the presence of flow or jets). This situation is very unfor-

8 Moreover the RCU reformats the data, which slightly alters the size [58].

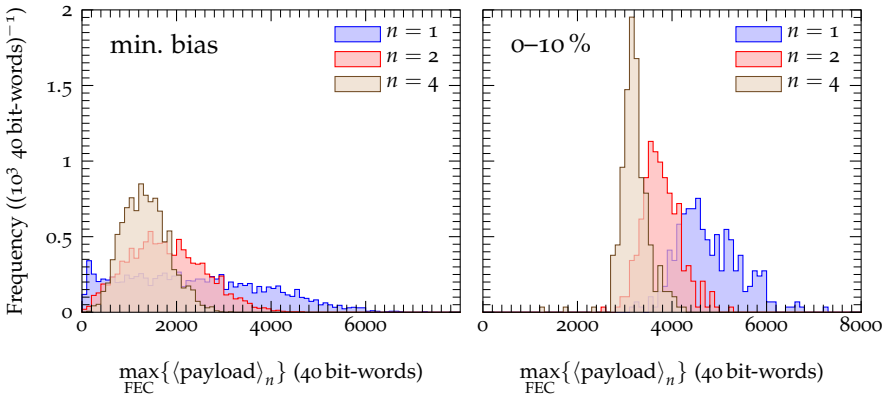

Figure 27: Distribution of maximum payload size for a FEC dependent on the number of MEB entries used. It is shown for min. bias (left) and 0–10 % central (right) $\sqrt{s_{\text{NN}}} = 2.76$ ATeV Pb–Pb events. The data size is normalised to one event and FEC. In addition to this payload each FEC transfers 128 trailer words.

tunate for the read-out because it has to wait for the slowest part of the system. In the design of the front-end this was anticipated and the effect is mitigated by employing a multiple-event memory (MEB)[9]. How this helps is illustrated in Fig. 27. What is shown there is the maximum read-out time of a FEC *after* averaging over n events (which obviously does not commute).

5.3 TIMING

5.3.1 *Time scales*

Compared to silicon detectors, TPCs are inherently slow. This has several reasons that will be discussed in the subsequent sections. In particular there are three different time scales that one has to take into account (here listed with ALICE-specific numbers):

- Drift time: the maximum time an electron needs to reach an end-plate: 94 µs (drift velocity: 2.65 cm/µs), also called "acquisition time". (In the rest of this thesis 100 µs is used for simplicity and also because this number varies with pressure/temperature a safety margin is needed.)

- Ion clearing time: the time it takes for the ions that were produced in the avalanches to be collected within the read-out chambers: 180 µs. [56]

9 There is a second reason to have the MEB, discussed in Sec. 5.3.3.

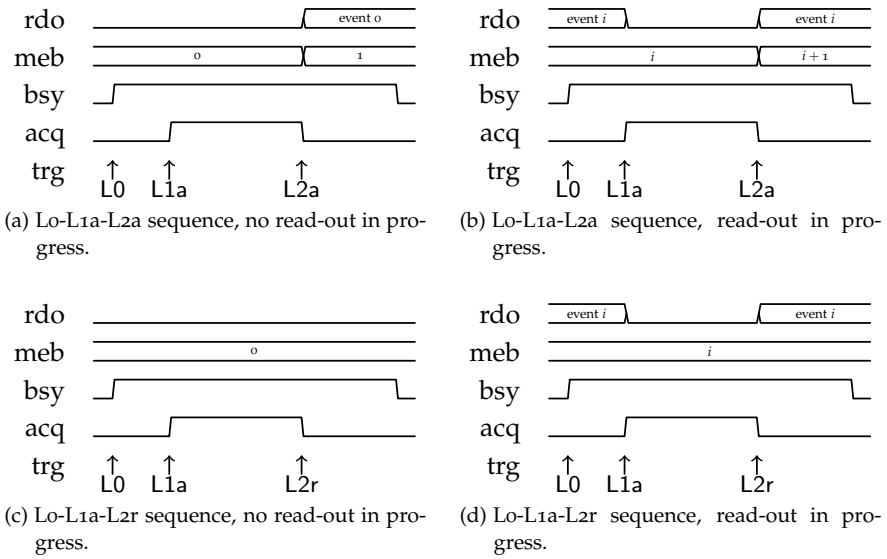

(a) Lo-L1a-L2a sequence, no read-out in progress.

(b) Lo-L1a-L2a sequence, read-out in progress.

(c) Lo-L1a-L2r sequence, no read-out in progress.

(d) Lo-L1a-L2r sequence, read-out in progress.

Figure 28: Example trigger sequences together with the state of the read-out.

- Read-out time: the time it takes to ship the data of one event off-detector: order of 1 ms (explained below).

Surely, the slowest time will determine the overall performance. In Sec. 5.5, however, a proposal is made that significantly decreases the read-out time. It will be shown that then all time scales will become of the same order and have to be considered equally.

5.3.2 *The ALICE trigger scheme*

Tailored to the presence of a TPC, ALICE uses a hierarchal sequence of three hardware and one software trigger [72]. They are issued with increasing latency with respect to the bunch crossing (BC) of the collision:

L0 "level zero", 1.2 µs after BC; very basic logic, e. g. interaction or centrality trigger.

L1 "level one", 7.7 µs after BC, if present (L1a, "level one accept") it starts the TPC acquisition, otherwise the trigger sequence is aborted; medium complexity, e. g. TRD di-electron trigger [75].

L2 "level two", about at least 100 µs after BC, validates (L2a, "level two accept") or invalidates (L2r, "level two reject") the event. Only if validated an event will be read out. Implements the "future part" of the past-future protection (more in the next section).

HLT "high level trigger", up to 1 kHz (Pb–Pb) and 2 kHz (p–p), latencies of a few seconds [76]. Triggers are based on a full software reconstruction of events.

Such a scheme makes sense, because the TPC's drift time can be seen as an event buffer and when sacrificing a few cm of drift time one may trigger its read-out later, allowing for more complex trigger decisions. This is employed by the L1 trigger in the above scheme: some 20 cm at the ends of the TPC are sacrificed to allow for a more complex event selection.

The TPC is acquiring data after each L1a for 100 µs. In order to keep the noise a at minimal level, the read-out is paused until the acquisition has finished (L2a or L2r). This is shown schematically in Fig. 28.

5.3.3 *Rate limits*

The trigger rates that the TPC is capable of dealing with, has inherent limitations that are not only determined by the time it needs to read out events. In this section different contributions to the dead time are analysed. This is done by assuming that events obey a Poisson process, i. e. that events are independent and appear after time intervals Δt distributed according to an exponential distribution with average interaction rate λ_{int}:

$$\Delta t \sim \exp(-\lambda_{\text{int}} \Delta t) \, . \tag{5.2}$$

In other terms, this approximation neglects discrete bunch structure of the LHC as well as the filling scheme. Furthermore, for simplicity, it shall be assumed:

$$\lambda_{\text{int}} \geq \lambda_{\text{Lo}} = \lambda_{\text{L1a}} \geq \lambda_{\text{L2a}} \, , \tag{5.3}$$

which essentially means that no L1 triggers are employed.

In the following paragraphs, the most relevant rate limitations are derived. They are summarised in Fig. 29 and will reappear as reference lines in the plots of the subsequent sections.

Drift time

The first limit is imposed by a fixed dead time: with the current read-out electronics an acquisition, once it has started, will always last for the full drift time, $T_{\text{drift}} \approx 100\,\mu\text{s}$. Only after the acquisition has ended the data will be read out (L2a) or will be discarded (L2r). Therefore the TPC cannot be triggered for T_{drift} after Lo and one has $T_{\text{dead,1}} = T_{\text{drift}}$.

Ion-feedback protection

If one also wants to protect all ions created while the gating grid of the read-out chambers is open and gas amplification happens from entering the drift volume,

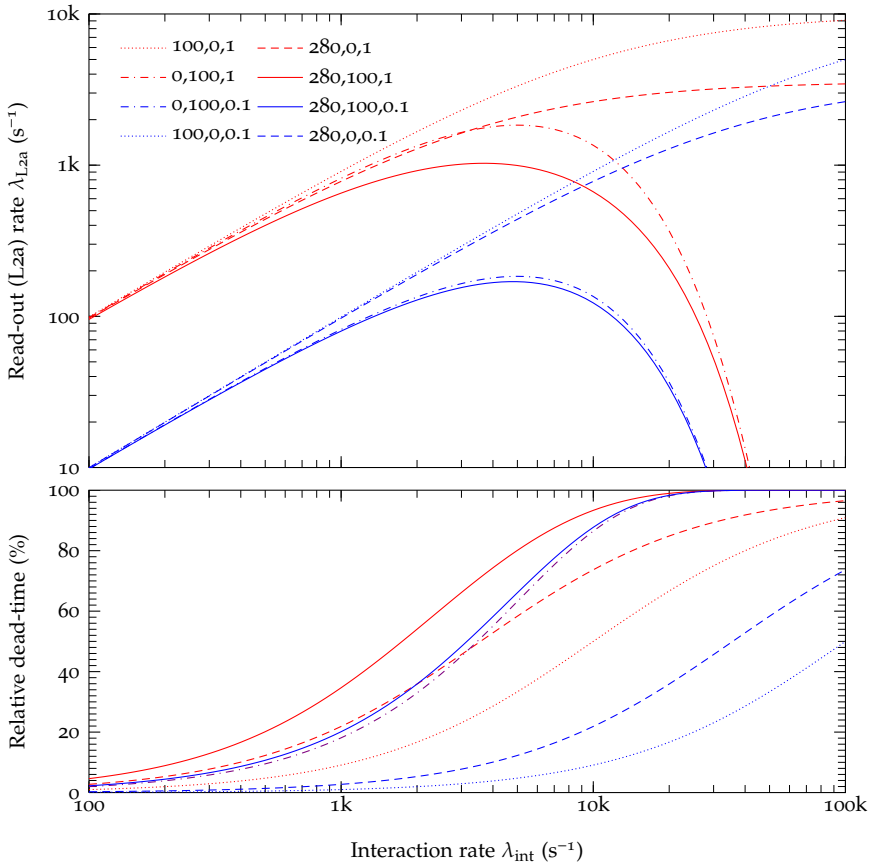

Figure 29: Theoretical rate limits for the TPC due to dead time and past-future protection. The numbers in the legend correspond to T_{dead},T_{PFP},ζ with times in µs. See text (Sec. 5.3.3) and Eq. 5.9 for an explanation of the parameters.

one needs to keep the gating grid closed for a fixed time (discussed in Sec. 5.5.1), $T_{dead,2} = T_{ion} \approx 180\,\mu s$ after each opening.

This determines the total dead time as $T_{dead} = T_{dead,1} + T_{dead,2} \approx 280\,\mu s$ and imposes a maximum read-out rate of $\lambda_{L2a,max} = T_{dead}^{-1} \approx 3.57 \times 10^3\,s^{-1}$ in the limit of infinite interaction rates, $\lambda_{int} \to \infty$.

When interaction rates are finite, however, a significant amount of triggers can become rejected. Employing the PASTA principle[10] it is easy to see that the average realative dead time T_{dead}/T will be:

$$\frac{T_{\text{dead}}}{T} = \frac{\lambda_{\text{Lo}} - \lambda_{\text{L2a}}}{\lambda_{\text{Lo}}} = \frac{1}{1+\varrho^{-1}} = \frac{1}{1+(\lambda_{\text{Lo}} T_{\text{dead}})^{-1}} \,, \tag{5.4}$$

where $\varrho = \lambda_{\text{Lo}}/\mu$ is the ratio of average input (trigger) rate and the mean processing rate. For fixed dead time the processing rate is constant, $\mu = T_{\text{dead}}^{-1}$.

Past-future protection

In order to only record events with tracks that can be reconstructed unambiguously a circuit known as "past-future protection" (PFP) may be employed. It rejects events that are not isolated by a certain time, $\pm T_{\text{PFP}}$, around the trigger time t_0.

The probability that no second event happens in the past $[t_0 - T_{\text{PFP}}, t_0]$ (or similar in the future $[t_0, t_0 + T_{\text{PFP}}]$) is given by the Poisson distribution:

$$P(n = 0, \lambda T_{\text{PFP}}) = \exp(-\lambda T_{\text{PFP}}) \,. \tag{5.5}$$

The two intervals before and after the trigger are independent, such that the probability to reject an event is:

$$P(\text{L2a}) = [\exp(-\lambda T_{\text{PFP}})]^2 \,, \tag{5.6}$$

which finally yields the trigger (L2a) rate λ_{L2a} as:

$$\lambda_{\text{L2a}} = \lambda_{\text{int}} \cdot P(\text{L2a}) = \lambda_{\text{int}} \exp(-2\lambda_{\text{int}} T_{\text{PFP}}) \,. \tag{5.7}$$

This function attains a maximum of $\lambda_{\text{L2a,max}} = (2T_{\text{PFP}})^{-1} \cdot e^{-1} \approx 0.18 (T_{\text{PFP}})^{-1}$ at $\lambda_{\text{int}} = (2T_{\text{PFP}})^{-1}$ and vanishes for small and large values of the interaction rate. In particular the case of $T_{\text{PFP}} = 100\,\mu\text{s}$ (i. e. only clean events without pile-up contributions) yields the maximum trigger rate of 1.8 kHz at an interaction rate of 5 kHz.

In the case that one only triggers on a fraction ζ of events (e. g. by selecting a centrality class), Eq. 5.7 changes to:

$$\lambda_{\text{L2a}} = \zeta\, \lambda_{\text{int}} \exp(-2\lambda_{\text{int}} T_{\text{PFP}}) \,, \tag{5.8}$$

since the protection is independent on the events one is triggering on.

In the case that dead time exists and PFP is enabled, an analog calculation yields:

$$\lambda_{\text{L2a}} = \zeta\, \lambda_{\text{int}} \exp(-2\lambda_{\text{int}} T_{\text{PFP}}) \frac{1}{1 + \zeta\, \lambda_{\text{int}} T_{\text{dead}} \exp(-\lambda_{\text{int}} T_{\text{PFP}})} \tag{5.9}$$

for $T_{\text{dead}} > T_{\text{PFP}}$ (otherwise the dead time is anyhow absorbed in the future protection). This is the most general result.

10 PASTA: Poissonian arrivals see time averages; see [77].

Multiple-event buffering

The read-out time of an event clearly also imposes a rate limit given by the read-out rate μ_{rdo}. A naive implementation makes the detector busy until an event has been read out. According to Eq. (5.4) this has dramatic consequences, since the read-out rate approaches its limit ($\lambda_{\mathrm{L2a,max}} = \mu_{rdo}$) only very slowly. In particular when the interaction rate equals the maximal read-out rate every second event gets rejected—even though enough bandwidth would be available to process all events.

The reason for this lies in the uncorrelated time distributions of event arrivals and read-out times. The situation can, however, be much improved by placing a buffer in the front-end electronics that decouples the acquisition of an event from its read-out, which is accomplished by the ALTRO multiple-event buffers.

5.4 TRIGGER-RATE SIMULATIONS

In the last section the considerations regarding the timing of the experiment were laid out using simplified models. Albeit being of high value conveying an intuitive picture, their validity is limited. Not only do they only define limiting values, but also do they completely neglect the precise topology of the events.

To overcome these restrictions a simulation of the trigger and read-out system was performed, that models the real set-up as closely as possible and uses measured read-out times from real events.

5.4.1 *Results*

The results of this simulation are shown in Figs. 30 and 31 The dependencies are shown for central and minimum bias $\sqrt{s_{\mathrm{NN}}} = 2.76\,\mathrm{ATeV}$ Pb–Pb events together with the theoretical limits from Fig. 29.

The opaque symbols show the read-out rates that can be achieved with min. bias ($534\,\mathrm{s}^{-1}$) and central ($318\,\mathrm{s}^{-1}$) Pb–Pb events.

In addition to the nominal settings, the open symbols in Fig. 30 show how the performance changes when past-future protection (PFP) can be disabled.

5.5 UPGRADE OF THE READ-OUT NETWORK

From Fig. 30 it becomes obvious that there is margin for improving the performance of the TPC. The read-out rate of 534 Hz is only defined by the electronics and even when requiring only one event in the TPC drift volume (past-future protection set to $\pm 100\,\mu\mathrm{s}$) an increase by a factor of two is feasible. A factor of ten could be achieved when loosening the requirements of the past-future protection as can be seen from Fig. 29.

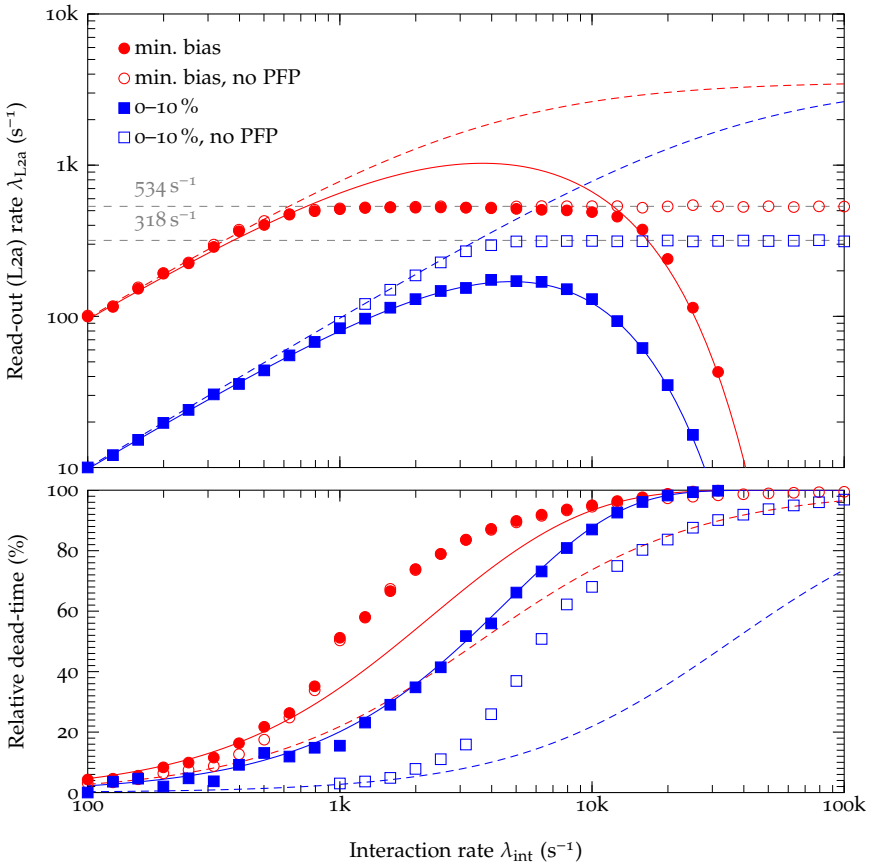

Figure 30: Simulated read-out rates and dead times for the current read-out. The lines denote the theoretical optima in case of vanishing read-out time and are the same of Fig. 29.

5.5.1 *Fundamental operational limitations*

The operation of a TPC has limitations that are intrinsic. This is due to the fact that its gas volume is always active, i. e. that particles of any event transversing it will also cause gas ionisation. All events are detected and thus overlaid in the drift volume. This yields three problems:

- Space charge: at some point the ionisation charge may not be neglected anymore when calculating the electric field inside the detector. The particle tracks are bent away in a complicated, event rate- and topology-dependent fashion. Details can be found in [56].

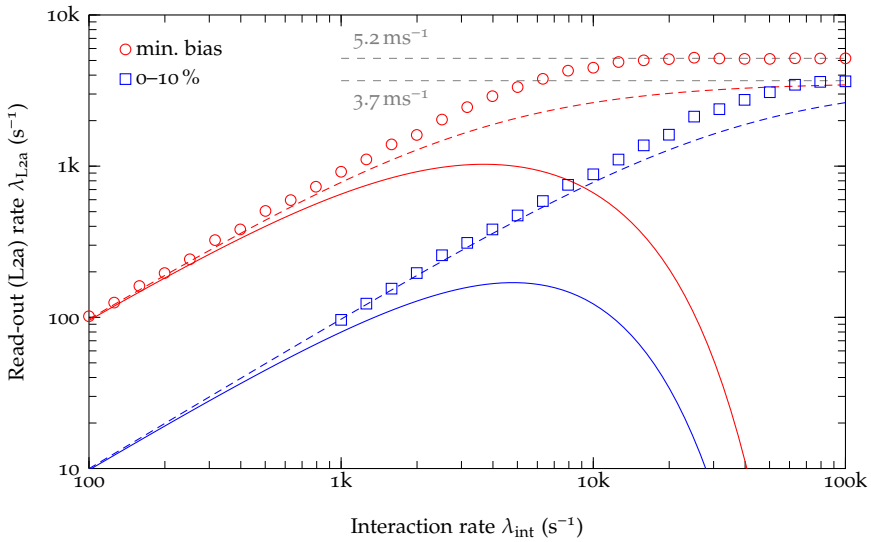

Figure 31: Simulated read-out rates for the upgrade proposal. The plotted points do only take into account the dead time due to the drift (100 µs) and thus ignore PFP and ion-protection. It can be seen that these would always be the limiting factor. The lines denote the theoretical optima in case of vanishing read-out time and are the same of Fig. 29.

- Track-event association: if two collisions happen after each other, tracks of the first one drift away towards the end-plates before the second collision happens. This makes them pointing to displaced origins that are away from the interaction point[11]. If the time between two collisions is however too small, they cannot be associated to the proper event anymore.

- Occupancy: at some point the detector becomes opaque, and tracks cannot be isolated anymore. But even before the resolution will degrade because the number of track crossings will increase and the crossing points cannot be used for tracking.

5.5.2 *Upgrade proposal*

The proposal for an upgrade of the read-out electronics for the TPC is based on a replacement of the electronics connecting the FECs to the outside world (DAQ, Trigger and DCS). It was initially based on simulations as no real Pb–Pb data was available [78].

11 Actually, tracks from side A will point to a vertex at positive z values, tracks from side C to negative z values.

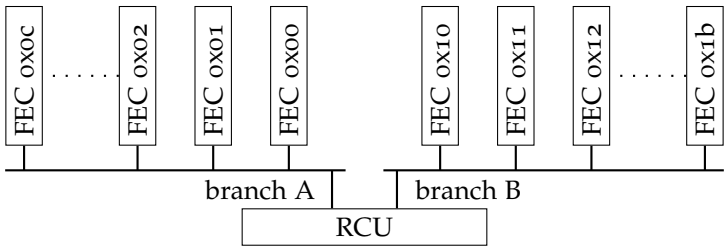

(a) Current (bus) topology.

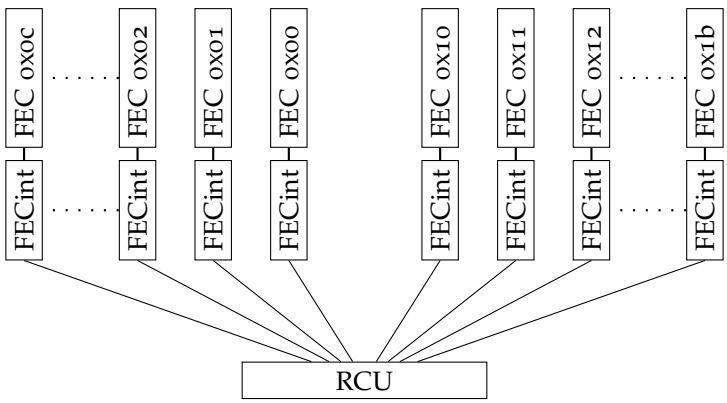

(b) Proposed (star) topology.

Figure 32: Topology of the read-out network. Here shown for read-out partition 1 with 25 FECs and the current numbering in hexadecimal notation.

With the current elctronics, one deals with a rather high protocol overhead at the moderate multiplicities ($\mathrm{d}N_{\mathrm{ch}}/\mathrm{d}\eta|_{\eta=0} \approx 1600$ for most central Pb–Pb collisions at $\sqrt{s_{\mathrm{NN}}} = 2.76\,\mathrm{ATeV}$ [17]) as observed. The design multiplicities were much higher and the protocol overhead not thought to be a limiting factor [21].

The main idea behind the upgrade is to replace the bus-based topology by a point-to-point star topology as depicted in Fig. 32. This can be achieved by using high-speed ($2.0\,\mathrm{Gbit/s}$[12]) serial links instead of 40 bit-wide parallel buses. In such a configuration the full bandwidth of a FEC can be utilised and no further speed reduction is imposed. Moreover, this can be achieved without replacing the FECs, which is a big advantage in terms of total cost.

5.5.3 *Prototype*

Such an upgrade consists of two main parts: an interface card that translates the FEC-bus to serial lines, and an RCU that gathers many serial links and provides the interface to the off-detector subsystems (Trigger, DAQ and DCS). While the

12 The peak bandwidth of the bus is $1.6\,\mathrm{Gbit/s}$, a 20 % overhead due to 8/10 bit encoding is assumed.

second part is rather straight forward, it has to be proven that an interface card can be engineered such that it is small and cheap enough.

Design considerations

The operation environment of the FECint card causes some design difficulties: it is supposed to be operated inside the magnetic field of the L3 magnet (0.5 T) and to be subjected to a considerable amount of radiation (both in terms of total dose and instantaneous flux [67]). While the first just dictates the use of linear voltage regulators (as opposed to switched ones[13]), the latter has some serious impact. All electronic components have to be carefully tested to survive the total expected dose and digital circuits need to be protected against single event upsets (SEUs). [67]

Large efforts were made to characterise the currently mounted electronics, and the RCU contains a circuit to make it reliable against SEUs. In the first years of LHC operation this turned out to be worth the effort. SEUs were measured right from the beginning, first in the ALTROs [61], then in the RCUs [66].

These measurements also show that the approach of using off-the-shelf electronics, characterising them for total dose and protecting them against SEUs is a successful design practise for these environments. This approach was followed in the design of the FECint as well.

The prototype was built to demonstrate:

- Electrical "interfacability": the FEC used GTL to communicate via the bus. This is not well suited for point-to-point connections due to the too high power consumption and the necessity of bus driver circuits. The latter show some additional and—even worse—model/manufacturer dependent latency, that even makes the 40 MHz timing critical. On the prototype standard CMOS was used to interface the GTL lines directly. No external driver chip was used.

- Mechanical feasibility: the available space at the TPC end-plates is very limited. Fitting additional electronics is only possible if it is slim enough.

- Cost: high-speed transceivers are expensive, especially when being placed on 4356 boards.

Prototype card

The prototype is based on a small FPGA (a Xilinx Virtex-II Pro[14]) that incorporates high speed serial links. Its I/O was directly connected to the FEC bus and the

13 Magnetic fields do not per se forbid switching regulators, but R&D in this field is just about to start, see e. g. [79].

14 While a Xilinx Spartan-6 [80] device was the model of choice, it was not available on the market and the Virtex II-Pro device [81] was the closest match.

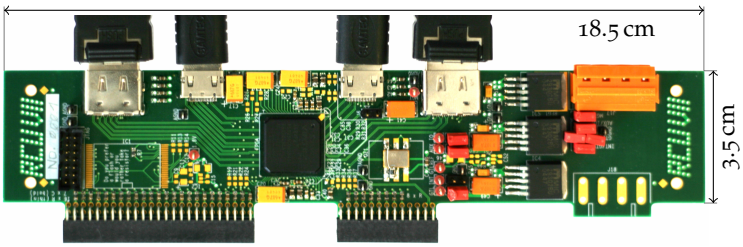

Figure 33: Picture of the FECint prototype (similar to[78]). Here printed to scale 1:2.

serial link was connected to HDMI[15] connectors. The resulting PCB was produced and assembled. It is depicted in Fig. 33.

A number of test features were implemented to carefully characterise its behaviour:

- All power supplies of the FPGA were routed separately, such that their currents can be monitored individually.
- Four serial ports were routed. Two were connected to HDMI, and two were connected to mini-HDMI connectors. Moreover, each pair of connectors has layouts with receive and transmit lines swapped such that a straight cable can be used to perform a loopback test.
- An FPGA temperature probe can be connected to monitor the heat dissipation of the circuit in different modes of operation.
- The FPGA firmware included a custom high speed bus analyser to monitor the precise timing on the digital data lines.

5.6 DISCUSSION

An upgrade of the TPC read-out electronics looks very promising in terms of higher read-out rates. With the proposed upgrade, the detector may be read-out ten times faster, which directly translates into physics yields.

However, there are surely other parts that could be improved as well: in particular the dead time could be reduced by closing the GG and possibly aborting an acquisition as soon as possible when a L2r condition is fulfilled.

15 HDMI "High Definition Multimedia Interface" is a consumer product connector standard for serial connections, developed vor display adapters

6

CONCLUSIONS AND OUTLOOK

It has been demonstrated that the detailed study of QGP requires very involved detectors. During the past first years of operation, the ALICE detector has shown to be able to record data at unprecedented rates and was able to perform precession measurements. However, there are also a number of measurements that are currently impossible or that would highly benefit from a detector with higher resolution or with the capability to record more events.

6.1 BENEFITS OF THE UPGRADE

An upgrade of the ALICE detector that improves position resolution and read-out rates gives access to many interesting physics measurements. In particular the presented case of the Λ_c^+ particle will allow to study many of the important aspects of charm production, interaction, and hadronisation.

Figure 34 for example shows how the upgraded detector would allow to check if there is an Λ_c^+ / D^0 enhancement similar to the observed Λ / K_S^0 enhancement.

6.1.1 *Other measurements*

Apart the Λ_c^+ case that was laid out in this thesis, many other measurements will also either benefit or become possible with the upgrade, like e. g. the D_s^+ mesons in Pb–Pb collisions. The line of argumentation is very similar to the Λ_c^+ case, but often a bit less demanding, which is mainly due to the very short decay length of the Λ_c^+ of 59.9 µm as e. g. compared to the D_s^+ case with 149.9 µm.

Another set of measurements is that of beauty hadrons that decay via charmed hadrons. The mass spectra of charmed hadrons typically have quite some (order of 10 %) entries from counting the decay products of beauty decays. Their contribution is highly dependent on the precise set of selection cuts that are applied. For example, the pointing angle cut disfavours charm from beauty, because the charmed mesons point to their production vertex, and typically not to the primary vertex (due to the momentum carried away by the other decay products of the beauty decay). Contrarily, the cut on the minimal decay length favours charm

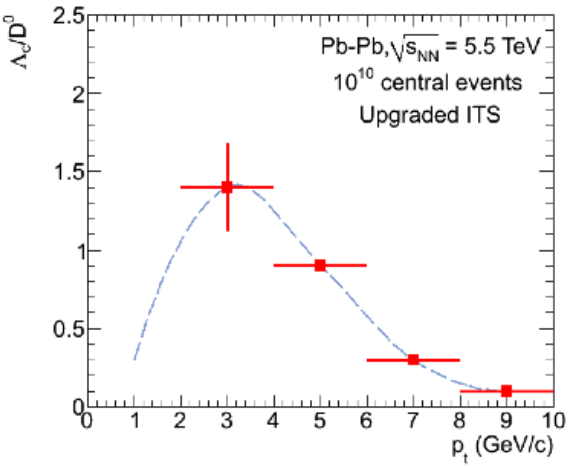

Figure 34: With 10^{10} events, ALICE would be able to detect a Λ_c^+ / D^0 enhancement similar to the Λ / K_S^0 case. The error bars show the statistical uncertainties of the Λ_c^+ yield extraction. Figure taken from [28].

hadrons from beauty, because already the beauty decays are displaced by some 450 µm to 500 µm. Better resolutions will help to disentangle the contributions and to measure the charm and beauty cross-sections independently and—more importantly—model-free.

6.1.2 *Future plans*

The LHC machine will be shut down for maintenance in 2013–2014 and 2017–2018 for roughly two years each. In the first period the ALICE TPC collaboration is currently evaluating to install an upgrade based on the proposal of Chap. 5. In 2017–2018 the ALICE ITS collaboration will replace their detector by a new one, which is meeting the requirements explored in Chap. 4. The presented work is a major contribution to both proposals.

A

KINEMATICS

A.1 $\Lambda_c^+ \to (\Sigma^0 \to \Lambda\gamma)\,\pi^+$

The mass difference $m_{\Sigma^0} - m_\Lambda = 76.959(35)\,\mathrm{MeV/c^2}$ is small and thus the photon carries away only a small fraction of total energy, leading to a visible contribution of this decay in the $\Lambda\pi^+$ mass spectra. The contributions is surely not peak-like but continuous and its shape is calculated hereunder.

If $m_{\Lambda\pi^+}$ denotes the mass reconstructed from the Λ and the π^+, then one gets:

$$\begin{aligned}\Delta m^2 &= m^2_{\Lambda\pi^+} - m^2_{\Lambda_c^+} = (p_{\pi^+} + p_\Lambda)^2 - p^2_{\Lambda_c^+} = (p_{\Lambda_c^+} - p_\gamma)^2 - p^2_{\Lambda_c^+} \\ &= -2p_{\Lambda_c^+} p_\gamma \,. \end{aligned} \tag{A.1}$$

This can best be evaluated in the Σ^0 rest frame:

$$p_{\Lambda_c^+} p_\gamma = E_{\Lambda_c^+} E_\gamma - |\vec{p}_{\Lambda_c^+}||\vec{p}_\gamma| \cos\vartheta = E_\gamma (E_{\Lambda_c^+} - |\vec{p}_{\Lambda_c^+}| \cos\vartheta) \,, \tag{A.2}$$

where ϑ is the angle between the Λ_c^+ and the γ in this frame.

Here, all parameters are fixed by the kinematics of the two body decays, such that the general relationship is of the form:

$$\Delta m^2 = a + b\cos\vartheta \,, \tag{A.3}$$

which is a mass shift with a smearing. For the allowed mass range this is reflected in the mass differential cross-section:

$$\frac{\mathrm{d}\sigma}{\mathrm{d}m_{\Lambda\pi^+}} = \frac{\mathrm{d}\sigma}{\mathrm{d}m^2_{\Lambda\pi^+}} \frac{\mathrm{d}m^2_{\Lambda\pi^+}}{\mathrm{d}m_{\Lambda\pi^+}} = \frac{\mathrm{d}\sigma}{\mathrm{d}\cos\vartheta} \left(\frac{\mathrm{d}m^2_{\Lambda\pi^+}}{\mathrm{d}\cos\vartheta}\right)^{-1} 2m_{\Lambda\pi^+} \propto m_{\Lambda\pi^+} \,, \tag{A.4}$$

where the isotropy of the decay enters. That is the yield is proportional to the mass within a fixed mass range.

This mass range can be calculated from the two two-body decays in the Σ^0 rest frame. From the $\Lambda_c^+ \to \Sigma^0\pi^+$ kinematics one obtains:

$$E_{\Lambda_c^+} = \frac{m^2_{\Lambda_c^+} + m^2_{\Sigma^0} - m^2_{\pi^+}}{2m_{\Sigma^0}} \tag{A.5}$$

$$|\vec{p}_{\Lambda_c^+}| = \frac{\left[\left(m^2_{\Sigma^0} - (m_{\Lambda_c^+} + m_{\pi^+})^2\right)\left(m^2_{\Sigma^0} - (m_{\Lambda_c^+} - m_{\pi^+})^2\right)\right]^{1/2}}{2m_{\Sigma^0}} \,, \tag{A.6}$$

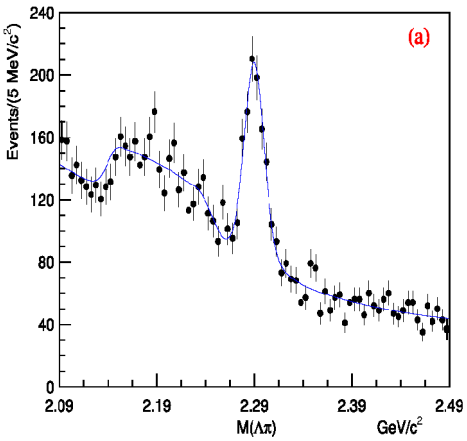

Figure 35: The $\Lambda\pi^+$ invariant mass spectrum of FOCUS. Left next to $\Lambda_c^+ \to \Lambda + \pi^+$ peak a broad structure that can be attributed to the decay $\Lambda_c^+ \to (\Sigma^o \to \Lambda\gamma) + \pi^+$ is observed. Figure from [82].

and from the $\Sigma^o \to \Lambda\gamma$:

$$E_\gamma = \frac{m_{\Sigma^o}^2 - m_\Lambda^2}{2m_{\Sigma^o}} \,. \tag{A.7}$$

One may simplify this expression by neglecting the pion mass:

$$E_{\Lambda_c^+} \approx \frac{m_{\Lambda_c^+}^2 + m_{\Sigma^o}^2}{2m_{\Sigma^o}} \tag{A.8}$$

$$|\vec{p}_{\Lambda_c^+}| \approx \frac{m_{\Lambda_c^+}^2 - m_{\Sigma^o}^2}{2m_{\Sigma^o}} \,, \tag{A.9}$$

which yield the final result in short form as:

$$m_{\Lambda\pi^+} \in \left[\frac{m_{\Lambda_c^+} m_\Lambda}{m_{\Sigma^o}} \,;\, \sqrt{m_{\Lambda_c^+}^2 + m_\Lambda^2 + m_{\Sigma^o}^2}\right] = [2.139; 2.247] \text{ GeV/c}^2 \tag{A.10}$$

This means that a trapezoidal structure with $\mathrm{d}N/\mathrm{d}m \propto m$ will appear in the mass range of $[2.139; 2.247]$ GeV/c². This will needs of course be folded with the detector response and corrected for the selection efficiency, but is essentially what is measured by FOCUS (Fig. 35).

REFERENCES

[1] P. Braun-Munzinger and J. Wambach. *Colloquium: Phase diagram of strongly interacting matter*. In: *Rev. Mod. Phys.* 81.3 (2009), pp. 1031–1050. DOI: 10.1103/RevModPhys.81.1031. arXiv:0801.4256 [hep-ph] (cit. on p. 2).

[2] W. Greiner, S. Schramm and E. Stein. *Quantum Chromodynamics*. Springer, 2007. ISBN: 9783540485346 (cit. on p. 1).

[3] J. Bartke. *Introduction to Relativistic Heavy Ion Physics*. World Scientific, 2009. ISBN: 9789810212315 (cit. on p. 1).

[4] W. Florkowski. *Phenomenology of Ultra-Relativistic Heavy-Ion Collisions*. World Scientific, 2010. ISBN: 9789814280662 (cit. on p. 1).

[5] J. Kapusta, B. Müller and J. Rafelski. *Quark-Gluon Plasma: Theoretical Foundations: An Annotated Reprint Collection*. Elsevier, 2003. ISBN: 9780444511102 (cit. on p. 1).

[6] A. Kisiel (for the ALICE Collaboration). *Femtoscopy of Pb–Pb and pp collisions at the LHC with the ALICE experiment*. In: *J.Phys.G* 38 (2011), p. 124008. arXiv:1109.5553 [nucl-ex] (cit. on p. 2).

[7] ALICE Collaboration. *Anisotropic flow of charged hadrons, pions and (anti-) protons measured at high transverse momentum in Pb–Pb collisions at* $\sqrt{s_{NN}} =$ 2.76 TeV. In: *pre-print* (2012). arXiv:1205.5761 [nucl-ex] (cit. on p. 2).

[8] R. Preghenella (for the ALICE Collaboration). *Spectra of identified hadrons with the ALICE detector in pp and Pb–Pb collisions at the LHC*. In: *pre-print* (2012). arXiv:1203.5904 [hep-ex] (cit. on p. 2).

[9] P. Collaboration. *Enhanced production of direct photons in Au+Au collisions at* $\sqrt{s_{NN}} = 200$ GeV *and implications for the initial temperature*. In: *Phys. Rev. Lett.* 104.13 (2010), p. 132301. DOI: 10.1103/PhysRevLett.104.132301. arXiv:0804.4168 [nucl-ex] (cit. on p. 2).

[10] H. Niemi et al. *Influence of the shear viscosity of the quark-gluon plasma on elliptic flow in ultrarelativistic heavy-ion collisions*. In: *Phys.Rev.Lett.* 106.21 (2011), p. 212302. DOI: 10.1103/PhysRevLett.106.212302. arXiv:1101.2442 [nucl-th] (cit. on p. 2).

[11] M. L. Miller et al. *Glauber modeling in high energy nuclear collisions*. In: *Ann. Rev. Nucl. Part. Sci.* 57 (2007), pp. 205–243. DOI: 10.1146/annurev.nucl.57.090506.123020. arXiv:nucl-ex/0701025 [nucl-ex] (cit. on pp. 2, 30).

[12] A. Andronic et al. *Statistical hadronization of heavy quarks in ultra-relativistic nucleus-nucleus collisions*. In: *Nucl. Phys. A* 789 (2007), pp. 334–356. DOI: 10.1016/j.nuclphysa.2007.02.013. arXiv:nucl-th/0611023 [nucl-th] (cit. on pp. 2, 9, 18).

[13] F. Becattini. *Production of Multiply Heavy Flavored Baryons from Quark Gluon Plasma in Relativistic Heavy Ion Collisions*. In: *Phys. Rev. Lett.* 95 (2 2005), p. 022301. DOI: 10.1103/PhysRevLett.95.022301 (cit. on p. 3).

[14] ALICE Collaboration. *Suppression of high transverse momentum D mesons in central Pb–Pb collisions at* $\sqrt{s_{NN}} = 2.76$ TeV. In: *pre-print* (2012). arXiv:1203.2160 [nucl-ex] (cit. on pp. 3, 6, 33, 34).

[15] L. Evans and P. Bryant. *LHC Machine*. In: *JINST* 3.8 (2008), S08001. DOI: 10.1088/1748-0221/3/08/S08001 (cit. on p. 4).

[16] ALICE Collaboration. *The ALICE experiment at the CERN LHC*. In: *JINST* 3.8 (2008), S08002. DOI: 10.1088/1748-0221/3/08/S08002 (cit. on p. 4).

[17] ALICE Collaboration. *Charged-Particle Multiplicity Density at Midrapidity in Central Pb-Pb Collisions at* $\sqrt{s_{NN}} = 2.76$ ATeV. In: *Phys. Rev. Lett.* 105.25 (2010), p. 252301. DOI: 10.1103/PhysRevLett.105.252301 (cit. on pp. 4, 58).

[18] ALICE TPC Collaboration. *The ALICE TPC, a large 3-dimensional tracking device with fast readout for ultra-high multiplicity events*. In: *Nucl. Instr. Meth.* A622.1 (2010), pp. 316–367. DOI: 10.1016/j.nima.2010.04.042. arXiv:1001.1950 [physics.ins-det] (cit. on pp. 4, 5, 43, 44).

[19] ALICE Collaboration. *ALICE: Physics Performance Report, Volume I*. In: *J. Phys. G: Nucl. Part. Phys.* 30.11 (2004), p. 1517. DOI: 10.1088/0954-3899/30/11/001 (cit. on p. 4).

[20] ALICE Collaboration. *ALICE Inner Tracking System (ITS): Technical Design Report*. ALICE-TDR-4 ; CERN-LHCC-99-012. Geneva: CERN, 1999. URL: http://cdsweb.cern.ch/record/391175 (cit. on pp. 4, 33).

[21] ALICE Collaboration. *ALICE time projection chamber: Technical Design Report*. CERN-OPEN-2000-183 ; ALICE-TDR-7 ; CERN-LHCC-2000-001. Geneva: CERN, 2000. URL: http://cdsweb.cern.ch/record/451098/ (cit. on pp. 4, 43, 58).

[22] ALICE Collaboration. *ALICE Time-Of-Flight system (TOF): Technical Design Report*. ALICE-TDR-8 ; CERN-LHCC-2000-012. Geneva: CERN, 2000. URL: https://cdsweb.cern.ch/record/430132 (cit. on p. 4).

[23] ALICE Collaboration. *ALICE Time-Of Flight system (TOF): addendum to the Technical Design Report*. Technical Design Report ALICE ALICE-TDR-8-add-1 ; CERN-LHCC-2002-016. Geneva: CERN, 2002. URL: http://cdsweb.cern.ch/record/545834 (cit. on p. 4).

[24] ALICE Collaboration. *ALICE: Physics Performance Report, Volume II*. In: *J. Phys. G: Nucl. Part. Phys.* 32.10 (2006), p. 1295. DOI: 10.1088/0954-3899/32/10/001 (cit. on pp. 5, 10, 37).

[25] M. Gagliardi (for the ALICE Collaboration). *Measurement of reference cross sections in pp and Pb–Pb collisions at the LHC in van der Meer scans with the ALICE detector*. In: *AIP Conf. Proc.* 1422 (2012), pp. 110–116. arXiv:1109.5369 [hep-ex] (cit. on p. 6).

[26] ALICE Collaboration. *Charged-particle multiplicity measurement in proton–proton collisions at $\sqrt{s} = 7$ TeV with ALICE at LHC*. In: *Eur. Phys. J.* C68 (2010), pp. 345–354. DOI: 10.1140/epjc/s10052-010-1350-2. arXiv:1004.3514 [hep-ex] (cit. on pp. 6, 30).

[27] C. Bianchin (for the ALICE Collaboration). *Measurement of D^0 v_2 in Pb–Pb collisions at $\sqrt{s_{NN}} = 2.76$ TeV with ALICE at the LHC*. In: *pre-print* (2011). arXiv:1111.6886 [hep-ex] (cit. on pp. 6, 17).

[28] ALICE collaboration. *Conceptual Design Report for the Upgrade of the ALICE ITS*. CERN-LHCC-2012-005, LHCC-G-159. Geneva: CERN, 2012. URL: http://cdsweb.cern.ch/record/1431539 (cit. on pp. 6, 7, 17, 34, 35, 41, 62).

[29] ALICE collaboration. *Upgrade Strategy for ALICE at High Rate*. Tech. rep. CERN-LHCC-2012-004 ; LHCC-G-158. Geneva: CERN, 2012. URL: https://cdsweb.cern.ch/record/1431536 (cit. on pp. 7, 41).

[30] K. Nakamura et al. *Review of Particle Physics*. In: *J. Phys. G Nucl. Partic.* 37.7A (2010), p. 075021. DOI: 10.1088/0954-3899/37/7A/075021 (cit. on pp. 9, 11, 12, 14).

[31] A. Andronic et al. *Statistical hadronization model predictions for charmed hadrons at LHC*. In: *e-print* (2007). arXiv:0707.4075 [nucl-th] (cit. on p. 9).

[32] ZEUS Collaboration. *Measurement of charm fragmentation ratios and fractions in photoproduction at HERA*. In: *Eur.Phys.J.* C44.3 (2005), pp. 351–366. DOI: 10.1140/epjc/s2005-02397-3. arXiv:hep-ex/0508019 [hep-ex] (cit. on pp. 10, 15, 16).

[33] ZEUS Collaboration. *Measurement of D^+ and Λ_c^+ production in deep inelastic scattering at HERA*. In: *JHEP* 2010.11 (2010), p. 9. DOI: 10.1007/JHEP11(2010)009. arXiv:1007.1945 [hep-ex] (cit. on pp. 10, 15, 16).

[34] H1 Collaboration. *Inclusive production of D^+, D^0, D_s^+ and D^{*+} mesons in deep inelastic scattering at HERA*. In: *Eur. Phys. J.* C38.4 (2005), pp. 447–459. DOI: 10.1140/epjc/s2004-02069-x. arXiv:hep-ex/0408149 [hep-ex] (cit. on p. 10).

[35] L. Gladilin. *Charm Hadron Production Fractions*. In: *e-print* (1999). arXiv:hep-ex/9912064v1 (cit. on pp. 10, 15).

[36] X.-N. Wang and M. Gyulassy. *HIJING: A Monte Carlo model for multiple jet production in pp, pA and AA collisions*. In: *Phys. Rev.* D44.11 (1991), pp. 3501–3516. DOI: 10.1103/PhysRevD.44.3501 (cit. on pp. 10, 36).

[37] R. Dalitz. *On the analysis of τ-meson data and the nature of the τ-meson*. In: *Philos. Mag.* 44.357 (1953), pp. 1068–1080. DOI: 10.1080/14786441008520365 (cit. on p. 12).

[38] LEBC-EHS Collaboration. *Λ_c production characteristics in proton–proton interactions at 400 GeV/c*. In: *Phys. Lett.* B199.4 (1987), pp. 462–468. DOI: 10.1016/0370-2693(87)90954-3 (cit. on p. 15).

[39] ACCMOR Collaboration. *Production of the charmed baryon Λ_c^+ in π^-Cu and K^-Cu interactions at 230 GeV*. In: *Phys. Lett.* B247.1 (1990), pp. 113–120. DOI: 10.1016/0370-2693(90)91058-J (cit. on p. 15).

[40] P. Sorensen and X. Dong. *Suppression of nonphotonic electrons from enhancement of charm baryons in heavy ion collisions*. In: *Phys. Rev.* C74.2 (2006), p. 024902. DOI: 10.1103/PhysRevC.74.024902. arXiv:nucl-th/0512042 [nucl-th] (cit. on p. 17).

[41] G. Martínez-García, S. Gadrat and P. Crochet. *Consequences of a Λ_c/D enhancement effect on the non-photonic electron nuclear modification factor in central heavy ion collisions at RHIC energy*. In: *Phys. Lett.* B663.1-2 (2008), pp. 55–60. DOI: 10.1016/j.physletb.2008.01.079,10.1016/j.physletb.2008.07.061. arXiv:0710.2152 [hep-ph] (cit. on p. 17).

[42] I. Belikov (for the ALICE Collaboration). *K^0_S and Λ production in Pb–Pb collisions with the ALICE experiment*. In: *pre-print* (2011). arXiv:1109.4807 [hep-ex] (cit. on p. 17).

[43] STAR Collaboration. *Strange and Multi-strange Particle Production in Au+Au Collisions at $\sqrt{s_{NN}} = 62.4$ GeV*. In: *Phys. Rev.* C83.2 (2011), p. 024901. DOI: 10.1103/PhysRevC.83.024901. arXiv:1010.0142 [nucl-ex] (cit. on p. 17).

[44] STAR Collaboration. *Mass, quark-number, and sqrt $\sqrt{s_{NN}}$ dependence of the second and fourth flow harmonics in ultra-relativistic nucleus–nucleus collisions*. In: *Phys. Rev.* C75.5 (2007), p. 054906. DOI: 10.1103/PhysRevC.75.054906. arXiv:nucl-ex/0701010 [nucl-ex] (cit. on p. 17).

[45] R. J. Fries, V. Greco and P. Sorensen. *Coalescence Models For Hadron Formation From Quark Gluon Plasma*. In: *Ann.Rev.Nucl.Part.Sci.* 58 (2008), pp. 177–205. DOI: 10.1146/annurev.nucl.58.110707.171134. arXiv:0807.4939 [nucl-th] (cit. on p. 17).

[46] ALICE Collaboration. *ALICE computing: Technical Design Report*. ALICE-TDR-012 ; CERN-LHCC-2005-018. Geneva: CERN, 2005. URL: https://cdsweb.cern.ch/record/832753 (cit. on p. 19).

[47] I. Belikov et al. *Bayesian Approach for Combined Particle Identification in ALICE Experiment at LHC*. In: *Proceedings of CHEP 2004*. 2004 (cit. on p. 20).

[48] F. Noferini. *Prior-Iteration*. private communication. 2011 (cit. on p. 21).

[49] S. Gorbunov and I. Kisel. *Reconstruction of decayed particles based on the Kalman filter*. CBM-SOFT-note-2007-003. 2007 (cit. on p. 21).

[50] D. E. Knuth. *Big Omicron and big Omega and big Theta*. In: *SIGACT News* 8.2 (1976), pp. 18–24. DOI: 10.1145/1008328.1008329 (cit. on p. 23).

[51] ALICE Collaboration. *Centrality Dependence of the Charged-Particle Multiplicity Density at Midrapidity in Pb-Pb Collisions at* $\sqrt{s_{NN}} = 2.76$ ATeV. In: *Phys. Rev. Lett.* 106.3 (2011), p. 032301. DOI: 10.1103/PhysRevLett.106.032301. arXiv:1012.1657 [nucl-ex] (cit. on p. 30).

[52] ALICE Collaboration. *Measurement of charm production at central rapidity in proton-proton collisions at* $\sqrt{s} = 7$ TeV. In: *JHEP* 1201 (2012), p. 128. DOI: 10.1007/JHEP01(2012)128. arXiv:1111.1553 [hep-ex] (cit. on pp. 33, 34).

[53] ALICE Collaboration. *Alignment of the ALICE Inner Tracking System with cosmic-ray tracks*. In: *JINST* 5.3 (2010), P03003. DOI: 10.1088/1748-0221/5/03/P03003. arXiv:1001.0502 [physics.ins-det] (cit. on pp. 33, 34).

[54] A. Mastroserio et al. *Simulation tools for the ALICE ITS upgrade*. ALICE internal note. 2012 (cit. on p. 35).

[55] A. Kalweit. *Production of light flavour hadrons and anti-nuclei at LHC*. PhD thesis. Technische Universität Darmstadt, 2012 (expected) (cit. on p. 43).

[56] S. Rossegger. *Simulation and Calibration of the ALICE TPC including innovative Space Charge Calculations*. PhD thesis. Graz, Austria: Institute of Theoretical and Computational Physics, University of Technology, 2009 (cit. on pp. 43–45, 50, 56).

[57] J. Wiechula. *Commissioning and Calibration of the ALICE-TPC*. PhD thesis. Frankfurt am Main, Germany: Fachbereich Physik, Goethe-Universität, 2008 (cit. on p. 43).

[58] A. U. Rehman. *Design, implementation, integration, full-scale verification and performance optimization of the data acquisition circuit of the ALICE TPC readout electronics*. PhD thesis. Bergen, Norway, 2012 (expected) (cit. on pp. 43, 46, 49).

[59] C. Horn et al. (for the ALICE TPC Collaboration). *Trigger-induced mechanical resonances of gating grid wires in the multi-wire proportional chambers of the ALICE TPC*. In: *Proceedings of TIPP 2011*. 2012 (accepted for publication in Phys. Procedia). DOI: 10.1016/j.phpro.2012.02.395 (cit. on pp. 43, 45, 73).

[60] M. Mager (for the ALICE TPC Collaboration). *Mechanical resonances in the read-out chambers of the ALICE TPC*. In: *Proceedings of ISSP 2011*. to be published in World Scientific, 2012 (cit. on pp. 43, 45, 73).

[61] M. Mager et al. (for the ALICE TPC Collaboration). *Measurement of single event upsets in the ALICE-TPC front-end electronics*. In: *Appl. Mech. Mater.* 110 (2011), pp. 4505–4511. DOI: 10.4028/www.scientific.net/AMM.110-116.4505. arXiv:1110.3232 [physics.ins-det] (cit. on pp. 43, 45, 59, 73).

[62] L. Rolandi, W. Riegler and W. Blum. *Particle Detection with Drift Chambers*. 2008. ISBN: 9783540766834 (cit. on p. 43).

[63] M. Mager, S. Rossegger and J. Thomas. *The Langevin equation expanded to 2nd order and comments on using the equation to correct for space point distortions in a TPC*. ALICE internal note, ALICE-INT-2010-016. 2010. URL: https://edms.cern.ch/document/1108138/1/ (cit. on p. 44).

[64] M. Mager, S. Rossegger and J. Thomas. *Composed correction framework for modeling the TPC field distortions in AliRoot*. ALICE internal note, ALICE-INT-2011-002. 2011. URL: https://edms.cern.ch/document/1113105/1 (cit. on p. 44).

[65] M. Mager. *Spatial Calibration of the ALICE TPC Field Cage and First Physics Ideas*. Diploma thesis. Technische Universität Darmstadt, 2008 (cit. on p. 44).

[66] K. Røed et al. *First measurement of single event upsets in the readout control FPGA of the ALICE TPC detector*. In: *TWEPP 2011*. 2012 (to be published) (cit. on pp. 45, 59).

[67] A. Morsch and B. Pastričák. *Radiation in ALICE Detectors and Electronic Racks*. ALICE internal note, ALICE-INT-2002-028. 2002. URL: https://edms.cern.ch/document/358706/1 (cit. on pp. 45, 59).

[68] H. K. Soltveit. *The preamplifier-shaper for the ALICE TPC-Detector*. ALICE internal note, ALICE-INT-2009-039, https://edms.cern.ch/document/1054232/1. 2009 (cit. on p. 45).

[69] R. Bosch et al. *The ALTRO chip: a 16-channel A/D converter and digital processor for gas detectors*. In: *Nuclear Science, IEEE Transactions on* 50.6 (2003), pp. 2460–2469. DOI: 10.1109/TNS.2003.820629 (cit. on p. 45).

[70] C. G. Gutiérrez. *Readout and control system for the ALICE TPC electronics*. PhD thesis. University of Cantabria, Spain, 2007 (cit. on p. 46).

[71] C. Soos, G. Rubin and S. Csaba. *ALICE DDL – Hardware Guide for the front-end Designers*. 1998. URL: http://cdsweb.cern.ch/record/689280 (cit. on p. 47).

[72] A. Bhasin et al. *Implementation of the ALICE Trigger System*. In: *Real-Time Conference, 2007 15th IEEE-NPSS*. 2007, pp. 1–8. DOI: 10.1109/RTC.2007.4382861 (cit. on pp. 47, 51).

[73] P. Chochula et al. *The ALICE detector control system*. In: *IEEE Trans.Nucl.Sci.* 57 (2010), pp. 472–478 (cit. on p. 47).

[74] T. Krawutschke. *A flexible and reliable embedded system for detector control in a high energy physics experiment*. In: *Field Programmable Logic and Applications, 2008. FPL 2008. International Conference on*. 2008, pp. 155–160. DOI: 10.1109/FPL.2008.4629924 (cit. on p. 47).

[75] J. Klein (for the ALICE Collaboration). *Triggering with the ALICE TRD*. In: *pre-print* (2011). arXiv:1112.5110 [nucl-ex] (cit. on p. 51).

[76] A. Szostak (for the ALICE Collaboration). *Operational Experience with the ALICE High Level Trigger*. In: *Proceedings of CHEP 2012*. 2012 (cit. on p. 52).

[77] R. Wolff. *Poisson arrivals see time averages*. In: *Oper. Res.* 30.2 (1982), pp. 223–231. DOI: 10.1287/opre.30.2.223 (cit. on p. 54).

[78] A. Junique et al. *Upgrade of the ALICE-TPC read-out electronics*. In: *Topical Workshop on Electronics for Particle Physics*. Vol. 5. 12. 2010, p. C12026. DOI: 10.1088/1748-0221/5/12/C12026 (cit. on pp. 57, 60).

[79] L. Feld et al. *DC-DC buck converters for the CMS Tracker upgrade at SLHC*. In: *JINST* 6.1 (2011), p. C01020. DOI: 10.1088/1748-0221/6/01/C01020 (cit. on p. 59).

[80] Xilinx Inc. *Spartan-6 Family Overview*. DS160 (v2.0). 2011. URL: http://www.xilinx.com/support/documentation/data_sheets/ds160.pdf (cit. on p. 59).

[81] Xilinx Inc. *Virtex-II Pro and Virtex-II Pro X Platform FPGAs: Complete Data Sheet*. DS083 (v5.0). 2011. URL: http://www.xilinx.com/support/documentation/data_sheets/ds083.pdf (cit. on p. 59).

[82] FOCUS Collaboration. *Study of Λ_c^+ Cabibbo favored decays containing a Λ baryon in the final state*. In: *Phys. Lett.* B624.1-2 (2005), pp. 22–30. DOI: 10.1016/j.physletb.2005.08.014. arXiv:hep-ex/0505077 [hep-ex] (cit. on p. 64).

ACKNOWLEDGEMENTS

I am gratefully acknowledging the support I have gotten during my PhD work by my two supervisors Prof. Peter Braun-Munzinger and Luciano Musa. Thank you very much for offering my this unique opportunity to carry out my studies at CERN under your supervision. I have especially appreciated your guidance, leaving me enough freedom to explore some "side projects" (in particular [59, 60] and [61]).

Furthermore special thanks go to Anton Andronic, Thorsten Kollegger, Christian Lippmann, Rosa Romita, and Kai Schweda for proof-reading this thesis. Your comments and suggestions were a big help and very reassuring.

Finally, working in the scientific environment of CERN, the most stimulating and excellent (though highly heterogeneous) place I have seen so far, has been extremely exciting. In particular I enjoyed the coffee discussions and chats with all of you. I am looking forward to continuing working with you!

DECLARATION OF OWN WORK / EIGENSTÄNDIGKEITSERKLÄRUNG

I hereby confirm that the presented thesis contains, unless explicitly marked otherwise, work carried out solely by myself. When work done by others is referred to, it is cited and appears in the references.
Furthermore, I confirm that I have not attempted to obtain a PhD, yet.

Darmstadt, June 2012 Magnus Mager

Ich versichere hiermit, dass diese Arbeit, soweit nicht explizit anderweitig gekennzeichnet, selbständing verfasst wurde. Stellen, die die Arbeit Anderer referenzieren, sind deutlich gekennzeichnet und in den Referenzen aufgeführt.
Zudem versichere ich, dass ich bisher noch keinen Promotionsversuch unternommen habe.

Darmstadt, Juni 2012 Magnus Mager